1-9-2023

A Cdh3-β-catenin-laminin signaling axis in a subset of breast tumor leader cells control leader cell polarization and directional collective migration

Priscilla Y Hwang

Jairaj Mathur

Yanyang Cao

Jose Almeida

Jiayu Ye

See next page for additional authors

Authors

Priscilla Y Hwang, Jairaj Mathur, Yanyang Cao, Jose Almeida, Jiayu Ye, Vasilios Morikis, Daphne Cornish, Maria Clarke, Sheila A Stewart, Amit Pathak, and Gregory D Longmore

Article

Developmental Cell

A Cdh3-β-catenin-laminin signaling axis in a subset of breast tumor leader cells control leader cell polarization and directional collective migration

Graphical abstract

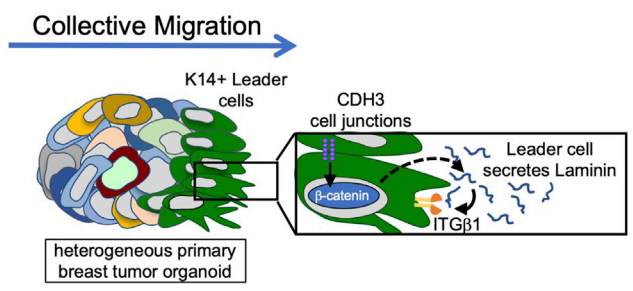

Highlights:

- In tumor collective migration there is leader cell heterogeneity which varies depending upon the signal.
- One subpopulation of leader cells (KRT14+/CDH3+) can direct collective migration.
- In leader cells at the leading edge, Cdh3-dependent cell-cell adhesions indirectly impact Integrin-dependent cell-matrix interactions and directional protrusions by local secretion of Laminin.

Highlights

- During collective migration breast tumor leader cells are heterogeneous
- A cadherin-3-positive subpopulation of leader cells can lead collective migration
- At the leading edge, cadherin-3 controls local laminin production to sustain integrin activity

Authors

Priscilla Y. Hwang, Jairaj Mathur, Yanyang Cao, ..., Sheila A. Stewart, Amit Pathak, Gregory D. Longmore

Correspondence

glongmore@wustl.edu

In brief

Hwang et al. describe how breast tumor leader cells develop and function to direct tumor collective migration and spread. In leader cells they find that cadherin-3 controls the local production of the basement membrane protein laminin at the leading edge to sustain collective migration.

Hwang et al., 2023, Developmental Cell *58*, 34–50
January 9, 2023
https://doi.org/10.1016/j.devcel.2022.12.005

CellPress

CellPress
OPEN ACCESS

Developmental Cell

Article

A Cdh3-β-catenin-laminin signaling axis in a subset of breast tumor leader cells control leader cell polarization and directional collective migration

Priscilla Y. Hwang,[1,5,6] Jairaj Mathur,[3] Yanyang Cao,[1,5] Jose Almeida,[4] Jiayu Ye,[2,5] Vasilios Morikis,[1,5] Daphne Cornish,[1,5] Maria Clarke,[1,5] Sheila A. Stewart,[2,5] Amit Pathak,[3,4] and Gregory D. Longmore[1,2,5,6,7,*]

[1]Departments of Medicine (Oncology), Washington University in St. Louis, St Louis, MO 63110, USA
[2]Departments of Cell Biology and Physiology, Washington University in St. Louis, St Louis, MO 63110, USA
[3]Departments of Mechanical Engineering and Materials Science, Washington University in St. Louis, St Louis, MO 63110, USA
[4]Departments of Biomedical Engineering, Washington University in St. Louis, St Louis, MO 63110, USA
[5]ICCE Institute, Washington University in St. Louis, St Louis, MO 63110, USA
[6]Department of Biomedical Engineering, Virginia Commonwealth University, Richmond, VA 23284, USA
[7]Lead contact
*Correspondence: glongmore@wustl.edu
https://doi.org/10.1016/j.devcel.2022.12.005

SUMMARY

Carcinoma dissemination can occur when heterogeneous tumor and tumor-stromal cell clusters migrate together via collective migration. Cells at the front lead and direct collective migration, yet how these leader cells form and direct migration are not fully appreciated. From live videos of primary mouse and human breast tumor organoids in a 3D microfluidic system mimicking native breast tumor microenvironment, we developed 3D computational models, which hypothesize that leader cells need to generate high protrusive forces and overcome extracellular matrix (ECM) resistance at the leading edge. From single-cell sequencing analyses, we find that leader cells are heterogeneous and identify and isolate a keratin 14- and cadherin-3-positive subpopulation sufficient to lead collective migration. Cdh3 controls leader cell protrusion dynamics through local production of laminin, which is required for integrin/focal adhesion function. Our findings highlight how a subset of leader cells interact with the microenvironment to direct collective migration.

INTRODUCTION

Collective migration is a process by which multiple cells move together in a coordinated manner and is essential during development and wound healing.[1–3] In disease states, such as cancer, collective migration is also important for tumor invasion and migration away from the primary tumor site leading to metastases.[4,5] Unlike single cell migration, collective migration requires that cells interact with neighboring cells as well as respond to environmental cues.[1,6,7] Within the extracellular matrix (ECM) surrounding tumors and in the circulating blood stream, tumor cells can be found in clusters. In the blood tumor cell clusters have up a 100-fold greater metastatic potential than single tumor cells.[8–11] Moreover, potently metastatic tumor cell clusters also contain stromal cells such as cancer-associated fibroblasts (CAFs) and immune cells,[9,12–15] and when stromal cells are present metastatic potential is further increased.[16,17]

Collectively migrating cells can be generally viewed as consisting of two populations: leader cells and follower cells.[18–21] Leader cells locate to the leading edge of migration while follower cells are at the rear. Many studies have characterized the cells at the leading edge, and it is now appreciated that leader cells explore their immediate microenvironment (chemical and physical), determine the direction of migration, generate traction forces necessary to move the whole, respond to and remodel their structural environment to facilitate invasion, and finally transmit signals to follower cells.[19,22] In breast cancer, leader cells have been histologically identified by the expression of the intermediate filament protein cytokeratin 14 (K14)[23–25] and in spontaneous mouse models of breast cancer, multicellular tumor clusters that contain K14+ cells have a higher propensity to metastasize.[24,26] Despite this, the full repertoire of molecular mechanisms driving leader cell formation and function in collective migration, and in which pathophysiologic context is not fully appreciated.

One hypothesis for breast tumor leader cell development posits that cells at the cluster edge, in contact with ECM, become leader cells in response to local microenvironmental cues.[22,27] In other study systems, K14+ cells within a breast tumor organoid can be randomly distributed and in response to hypoxia and signaling gradients migrate within the cluster to the leading edge (i.e., polarize to the leading edge) without apparent change in cell fate or number, despite being surrounded by ECM.[28] These observations suggest that leader cells

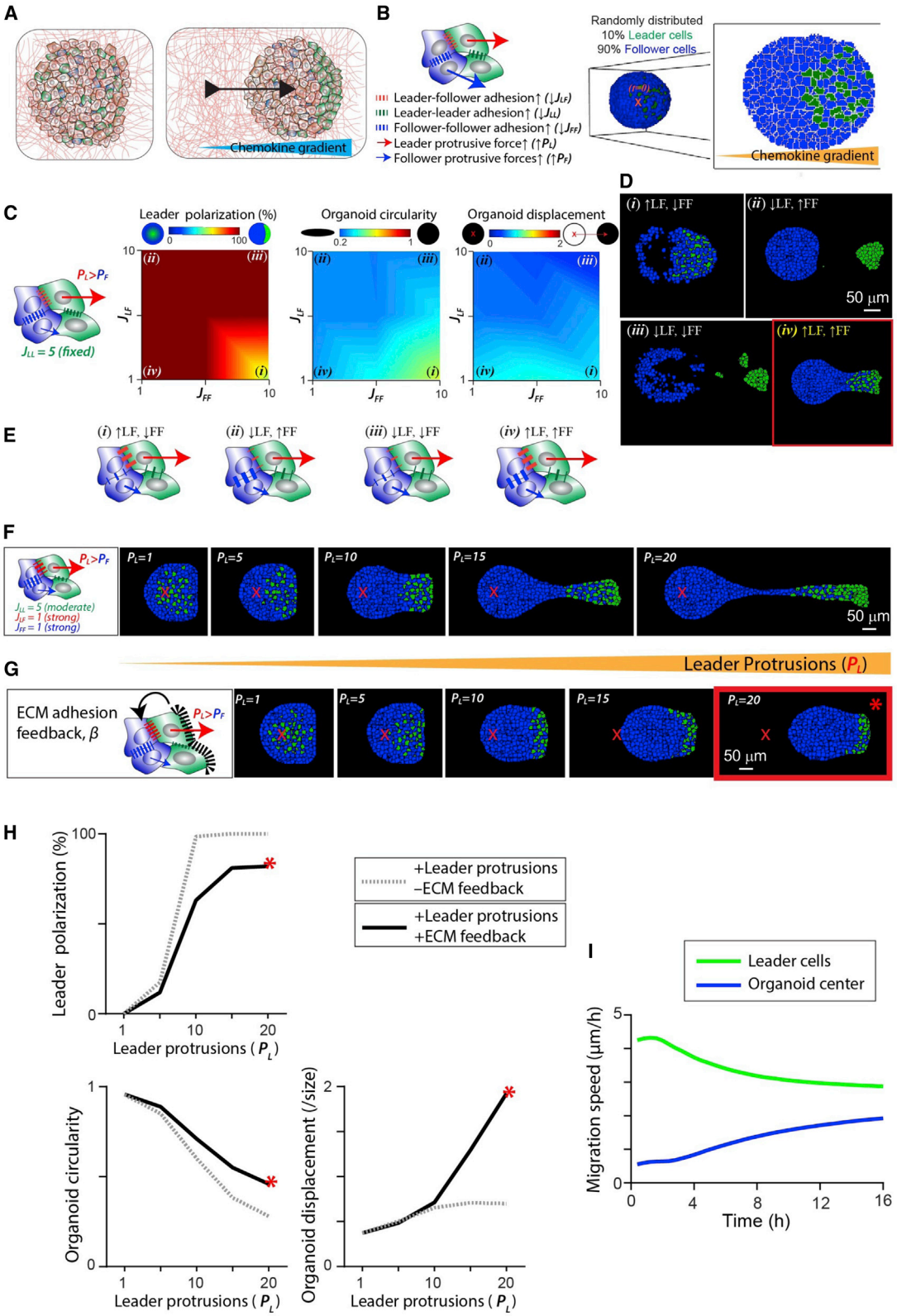

Figure 1. Computational modeling of tumor organoid collective invasion in 3D

(A) Schemes describing 3D tumor organoid response to a chemokine gradient (SDF1).

(B) Key modeling variables: leader/follower adhesions and protrusions (left). Leader cells (green) and follower cells (blue) in 3D (right).

(legend continued on next page)

could be more heterogeneous than previously appreciated, exhibit complex and perhaps differential responses to environmental signals, and behave distinctively from follower cells. Experiments studying collective invasion or migration, *ex vivo*, typically expose cells to uniform environmental signals and ambient oxygen concentration, which do not necessarily reflect *in vivo* exposure.[29] The cellular, chemical, and physical tumor microenvironment is extremely dynamic.[30–32]

To address these concerns, we made use of an *ex vivo* 3D microfluidic system and genetically defined breast tumor organoids derived from a metastatic mouse spontaneous genetic model (Mouse Mammary Tumor Virus LTR driven Polyoma Middle T antigen expression [MMTV-PyMT]) and a human metastatic breast cancer patient-derived xenograft (PDX) (human in mouse) model as these incorporate native tumor cell heterogeneity as well as tumor associated stromal cells. Tumor organoids are exposed to hypoxia (<2%) and environmental signaling gradients within a 3D collagen I matrix.[28] To gain insights into cellular behaviors that facilitate leader cells polarization to the leading edge and lead directed collective migration, we performed computational simulations based upon observations from published live videos.[28] To determine the cellular heterogeneity of leader cells and gain molecular and signaling pathway insights during active collective migration we performed single-cell RNA sequencing (scRNA-seq) analysis of collectively migrated tumor organoids. Informed by these results from we experimentally test hypotheses generated from precedent computational modeling.

We identify K14+ "leader" cell heterogeneity that differs depending upon the environmental signal. We isolate a subset of tumor leader cells that can lead collective migration of non-migratory normal breast organoids. These leader cells are enriched for cadherin-3 (Cdh3), and Cdh3 is required for both leader cell polarization and collective migration of the whole. In leader cells, Cdh3 controls protrusion dynamics and overcomes ECM resistance to migration by controlling transcription and local production of the basement membrane component laminin at the leading edge.

RESULTS

Computational modeling of tumor organoid collective migration in 3D predicts for leader cells with high protrusive forces and ECM adhesion feedback

To gain insight and generate experimentally testable hypotheses into how leader cells polarize to the leading edge and direct collective migration, we developed theoretical and computational models of tumor organoid migration in 3D. Simulation of whole organoid movement were calibrated against published videos of genetically labeled leader cells (K14-Actin.GFP) in mouse MMTV-PyMT breast tumor organoids that collectively migrate in hypoxia (<2%), through 3D collagen I matrixes, and in response to a Stromal cell-derived factor 1 (SDF1) chemical gradient.[28]

We used a lattice-based modeling approach with energy functionals to define cell types, adhesions, and protrusive forces (Figure 1B). In spatiotemporal simulations, stochastic movements follow energy-minimization criterion calculated over defined Monte Carlo steps (details in STAR Methods). We modeled organoids based on 10% K14+ leader cells in tumor organoids: leader cells (green) mixed randomly with follower cells (blue) and a rightward chemokine gradient (Figures 1A and 1B). From analyses of live movies, we observed three key phenotypes: (1) leader cell polarization to the migratory front, (2) organoids stay intact and retain circular shape, and (3) net organoid displacement toward the direction of chemokine gradient. In our simulations, we calculated these three readouts and calibrated them against the experimental video observation of breast tumor organoid collective migration in 3D.

First, we computationally tested whether differential leader and follower cell adhesions could explain leader cell polarization and organoid migration. We systematically varied leader-follower (J_{LF}), follower-follower (J_{FF}), and leader-leader adhesions (J_{LL}), while keeping leader and follower protrusions the same $P_L = P_F = 1$. There was no combination of cell-cell adhesions that alone could generate leader cell polarization (Figure S1A; Video S1A). Thus, we hypothesized that leader cells need to generate higher protrusions compared with follower cells, which we implemented via higher values of leader cell protrusive force ($P_L = 20$). With higher protrusive force, leader cell polarization increased for all values of J_{LL}, J_{FF}, and J_{LF} (Figure 1C; Figures S1B and S1C). We concluded that higher protrusive forces were important for the leader cells to move through the organoid and polarize to the invasive front, as observed in live videos. However, for most combinations of cell adhesions, organoid circularity and displacement remained low (Figure 1C; Figures S1B and S1C): i.e., organoids did not move or stay intact as leader cells polarize.

To better understand the contributions of leader-follower and follower-follower adhesions, we performed parametric scans for various combinations (details in STAR Methods). When either leader-follower or follower-follower adhesions were weak, organoid integrity was compromised and follower cells scattered or leader cells left the organoid after polarization (Figures 1C and 1Di–1Diii; Videos S1B, S2A, and S2B). When both leader-follower and follower-follower adhesions were strong, the organoid

(C) Heatmaps for leader cell polarization (left), organoid circularity (middle), and organoid displacement relative to initial radius (right) for varying J_{LF} and J_{FF}, leader-leader adhesions moderate ($J_{LL} = 5$), and leader cell protrusive forces high ($P_L = 20, P_F = 1$).

(D) Cross-section views of 3D organoid at t = 4 h for high leader cell protrusive forces and varying adhesions: (Di) weak follower-follower ($J_{FF} = 10$) and strong leader-follower ($J_{LF} = 1$); (Dii) strong follower-follower ($J_{FF} = 1$) and weak leader-follower ($J_{LF} = 1$); (Diii) weak follower-follower ($J_{FF} = 10$) and weak leader-follower ($J_{LF} = 10$); and (Div) strong follower-follower ($J_{FF} = 10$) and strong leader-follower ($J_{LF} = 10$).

(E) Schemes describing 4 cases in (D).

(F) Cross-section views of 3D organoid at t = 16 h for increasing P_L. X marks the initial position of organoid center.

(G) With ECM adhesion feedback present cross-section views of 3D organoid at t = 16 h for increasing P_L. Red outline and "*" symbol mark the case which captures video observation.

(H) Without ECM adhesion feedback (dotted line) and with ECM adhesion feedback (solid line) leader cell polarization, organoid circularity, and organoid displacement relative to organoid radius are plotted for varying leader protrusions P_L.

(I) Average leader population speed (green line) and average follower population speed (blue line) over time.

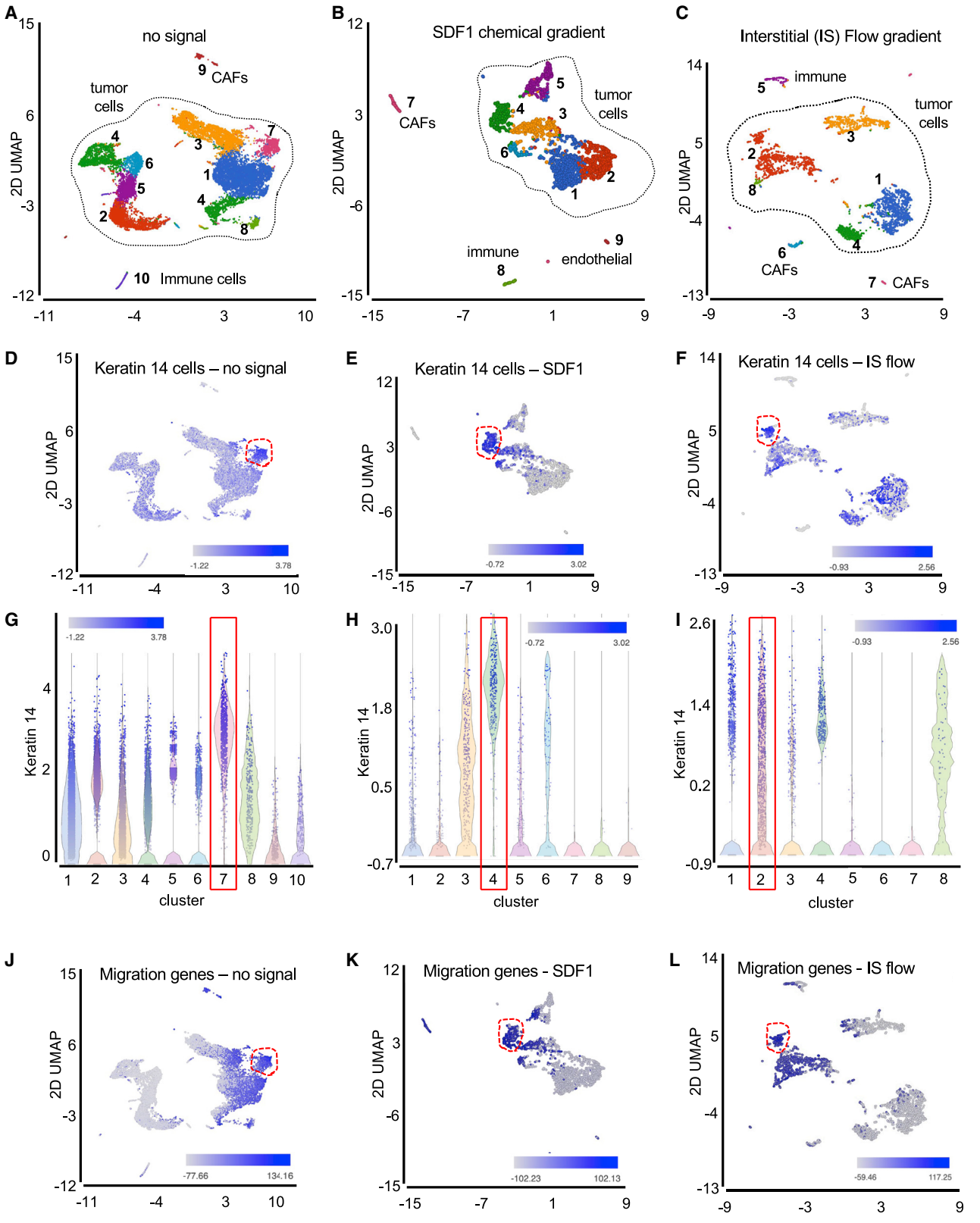

(legend on next page)

remained intact, leader cells polarized, and did not exit the organoid (Figures 1C and 1Div; Video S3A), yet organoid displacement remained low. With progressively higher leader protrusions (P_L), we predicted increased leader cell polarization, decreased organoid circularity, and increased organoid displacement (Figures 1F and 1H). However, even for the highest value of $P_L = 20$, organoid movement was minimal despite its elongation (Figures 1F and 1H; Video S3B). Stronger cell-ECM adhesions predicted for reduced organoid integrity; however, no values allowed for organoid displacement (Figure S1D).

Although preferential protrusions in leader cells moved them to the front, this polarization had no functional advantage for movement of the rest of the organoid. After leader cells arrive at the front, one key change is the presence of ECM, which is less inside the organoid. To understand the functional advantages of leader cell polarization, we hypothesized that upon reaching the front leader cells form new adhesions. This signal would reduce the energy barrier imposed by surrounding collagen fibers at the leading edge, be spatially restricted to the leader cells at the leading edge, and not occur when leader cells are embedded within the organoid. Since follower cell movement depends on leader cells, due to organoid cohesivity, feedback generated by leader cells could also indirectly enhance follower motility: i.e., collective organoid movement. We defined this signal in leader cells at the leading edge as "ECM adhesion feedback" and was implemented as parameter β (details in STAR Methods).

With added ECM adhesion feedback, we again performed simulations with varying leader protrusive forces (Figure 1F). For $P_L < 5$, there was little change in the organoid configuration, leader cell polarization, circularity, and net organoid displacement (Figures 1G and 1H). For higher values ($P_L > 5$), one key advantage was that the organoid circularity was maintained even as the leader cell polarization increases. For $P_L = 20$, the organoid traveled 2 times its radius in 16 h, which matched video observation (Figures 1G and 1H; Video S4), but weaker cell-ECM adhesions reduced organoid displacement (Figure S1E). This final simulation (annotated by an asterisk in Figures 1G and 1H) captured video observations per all three criteria of leader cell polarization, organoid circularity, and collective organoid movement. For preferential leader protrusions and active ECM adhesion feedback, average leader cell speed starts at a higher point relative to the rest of the organoid. The speed of the whole organoid catches up as leader cells reach the front (Figure 1I), which was consistent with live video observation.[28]

Based on this stepwise modeling approach, we make the following predictions for leader cell polarization and collective organoid movement through 3D collagen: (1) leader cells should have preferential protrusions relative to other cells (followers), (2) at least a subpopulation of leader cells form active ECM adhesions upon arriving at the front in order to reduce initial resistance presented by collagen, and (3) differential cell-cell adhesions of leaders and followers alone does not explain collective migration.

Collectively migrating mouse PyMT breast tumor organoids exhibit leader cell heterogeneity

To gain insight into molecular regulation of leader cell function, we performed scRNA-seq of mouse PyMT breast tumor organoids in hypoxia for 48 h (no signal) and after they had migrated collectively in response to a SDF1 gradient or interstitial (IS) flow gradient. Assessment of published cell-type markers identified ten distinct cell clusters in no signal, nine in response to SDF1, and eight in response to IS flow (Figures 2A–2C; Figures S2A–S2C). There were nine, six, or five tumor cell clusters, respectively, a single cluster of endothelial cells, and a single myeloid/immune cell cluster. In each sample there were two distinct CAF clusters: vascular CAFs and mesenchymal CAFs.[33] Developmental CAFs,[33] if present, were interspersed within the tumor cell populations.

Prior to exposure to migratory signals, K14 expression (leader cells) was distributed throughout all tumor cell clusters (Figures 2D and 2G). In response to SDF1 three of six tumor cell populations were enriched for K14 (Figures 2E and 2H), while in response to IS flow all five tumor cell populations expressed K14 (Figures 2F and 2I). To increase resolution and define K14+ subpopulations, we probed with known gene sets from GSEA. One had high expression of cell proliferation markers (Figure S2D). All were enriched for hypoxia responsive genes (Figure S2E). Genes important for cell migration were expressed in all K14+ clusters, as well as CAFs (Figures 2J–2L). A set of genes enriched in K14+ tumor cells from a primary mouse PyMT tumor (e.g., desmosomes and hemi-desmosomes)[24] revealed that cluster seven of no signal, cluster four of SDF1, and cluster two of the IS flow could be of particular importance (Figures 2D–2I, red outlines; Figure S2F).

These molecular analyses indicated that there was significant K14+ tumor cell molecular heterogeneity in collectively migrating breast tumor organoids. Leader cell heterogeneity varied depending upon the applied signal. In each sample there was a unique cluster of K14+ tumor cells that exhibited genomic features associated with migration-capable leader cells.

Cdh3 expression identifies a leader cell subpopulation capable of mediating collective migration

Are all K14+ tumor cells capable of leading tumor collective migration? Volcano plots comparing K14+ cluster 7 in no signal, cluster 4 in SDF1, and cluster 2 in IS flow with all other K14+ tumor cell clusters for each respective sample were performed (Figures 3A–3C). Results from all three experimental conditions were combined and a Venn diagram generated (Figure 3D; Table S1). 160 expressed genes were common between the three K14+ clusters. Within this group we asked which cell surface proteins, known to be associated with tumor progression, were present. The rationale was to use existing antibodies to isolate viable subpopulations of K14+ cells by flow cytometry. Candidates included Cdh3, Jag2, Fgfr2, and

Figure 2. scRNA-seq analysis of collectively migrated mouse breast tumor organoids

(A–C) UMAP plots of mouse MMTV-PyMT breast tumor organoids before migration (no signal) (A); after migration in a SDF1 gradient (B), or an interstitial (IS) flow gradient (C).

(D–I) (D–F) UMAP plots and violin plots (G–I) of K14 expression. Red outlines in each setting identify predominant K14 expressing tumor cell cluster.

(J–L) UMAP plots showing cell clusters expressing migration gene set. Red outlines identify tumor cell cluster co-enriched for K14 and migration genes. For scRNA-seq experiments, n = 3 biological replicates.

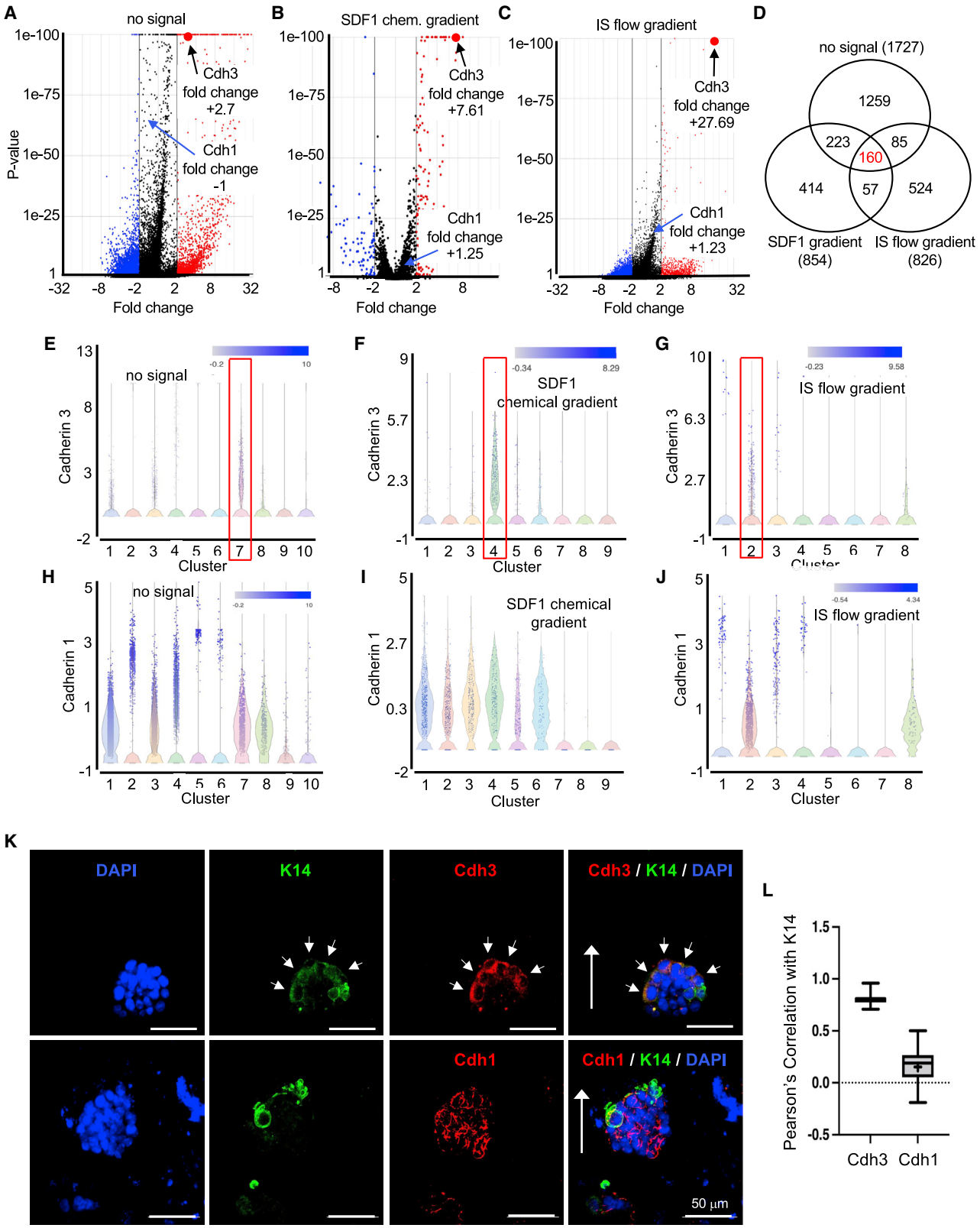

(legend on next page)

Cntfr. Cdh3, or P-cadherin, was of particular interest as volcano plots (Figures 3A–3C) and violin plots (Figures 3E–3G) revealed significant enrichment in all samples. Cadherin-1 (Cdh1), similar to Cdh3, is a well-known epithelial cell-cell adhesion molecule that plays a significant role in breast cancer invasion and metastasis.[34,35] In contrast to Cdh3, Cdh1 expression was distributed throughout all tumor cell clusters (Figures 3H–3J) and not enriched in Cdh3+ leader cell subpopulations (Figures 3A–3C).

We confirmed expression patterns of Cdh3 and Cdh1 in migrating mouse PyMT tumor organoids via immunostaining. Cdh3 protein was restricted to K14+ cells at the leading edge (Figures 3K and 3L). In contrast, there was little Cdh1 protein present in K14+ cells at the leading edge, rather Cdh1 was predominantly in K14− cells (Figures 3K and 3L). FACS analysis of dissociated mouse PyMT breast tumors revealed a Cdh3/K14 double positive tumor cell population (Figure S2G). Very few Cdh3+ cells were K14 negative (1.9%) (Figure S2G).

To test whether this K14+/Cdh3+ subpopulation of tumor cells could lead collective migration, we developed an invasive breast organoid reconstitution assay (Figure 4A). Organoids isolated from the breast of normal age-matched non-tumor-bearing mice are referred to as mammary gland organoids (MG). When MG were placed in our microfluidic platform and treated with SDF1, there was no K14+ cell polarization or collective migration (Figures 4B–4E). Next, K14+/Cdh3+ cells (CD45− and CAF−) were isolated from K14-Actin.GFP; PyMT breast tumors by flow cytometry. This population of tumor cells was mixed with MGs in ratios based on previously determined percentages (10% K14+ cells). Immunofluorescent analysis confirmed that reconstituted organoids had similar composition of K14+ cells as tumor organoids (Figure S2H). Added K14+/Cdh3+ cells were initially randomly distributed around the MG and in response to SDF1 polarized to the leading edge (Figure S2I), such as in PyMT breast tumor organoids. We refer to these reconstituted organoids as "MG + K14+/Cdh3+."

When MG + K14+/Cdh3+ organoids were added to the microfluidic platform and exposed to SDF1 K14+ cells polarized to a leading edge and directed collective migration (Figures 4B and 4C; quantified in Figures 4D and 4E). In control experiments, MGs reconstituted with $K14^{low}$/Cdh3− tumor cells did not migrate (Figures 4D and 4E). The presence of the fibrillar collagen receptor discoidin domain receptor 2 (DDR2) in K14+ PyMT tumor cells is required for collective migration[28] and lung metastasis.[36] In another control, MGs were reconstituted with K14+/Cdh3+ cells from $Ddr2^{-/-}$, PyMT breast tumors. In this setting, directional collective migration did not occur (Figure 4C; quantified in Figures 4D and 4E). Deletion of Ddr2 in PyMT tumors did not affect the scRNA-seq K14+ tumor cell profile nor Cdh3 expression (Figure S2J).

In sum, these results demonstrated that a K14+/Cdh3+ breast tumor cell subpopulation could lead directed collective migration of normal breast organoids through a 3D collagen I matrix.

Cdh3 expression is required for leader cell function

Cdh3 expression in cancer is associated with invasive behavior and poor clinical outcomes.[37,38] Cdh3 overexpression can promote collective cell migration.[39] Cdh3, in contrast to Cdh1, co-localized with K14+ cells at the leading edge and was not expressed by follower tumor cells (Figures 3K and 3L). This led us to ask whether breast cancer required Cdh3 for collective migration and how.

We identified distinct mouse and human Cdh3 shRNA lentiviruses that efficiently (>90%) depleted Cdh3 in mouse (4T1) and human (BT549) breast tumor cells as well as mouse PyMT and human PDX breast tumor organoids (Figures S3A–S3D). Depletion of Cdh3 in 4T1 and BT549 cells decreased their invasion through Matrigel and migration through 3D collagen I (Figure S3E). The lentiviral vectors expressed red fluorescent protein (RFP) (mouse) or GFP (human) that allowed for identification, tracking, and quantification of transduced cells (Figures S5B and S5D). Depletion of Cdh3 in both mouse (Figures 5A and 5B) and human (Figures 5C and 5D) breast tumor organoids resulted in decreased migratory efficiency and average migratory velocity. In Cdh3-depleted mouse, PyMT tumor organoids K14+ cells did not polarize to the leading edge (Figures 5E and 5F). In another approach, mouse PyMT breast tumor organoids were depleted of Cdh3 and placed in 3D collagen I breast tumor organoid cultures containing uniform concentration of bFGF + EGF (i.e., no gradient) and normoxia.[28] Under these conditions organoids send out circumferential invasive cellular projections led by K14+ leader cells yet the whole does not migrate.[24] We scored invasive phenotype (see examples Figures S3G and S3H) of tumor organoids, ±Cdh3. Depletion of Cdh3 resulted in decreased number of invasive tumor organoids (Figure S3I). To determine whether Cdh3 expression was required for *in vivo* lung metastases, we performed syngeneic, orthotopic breast transplant experiments with mouse 4T1 breast tumor cells, ±Cdh3. 4T1 cells express K14 and Cdh3. There was no difference in primary tumor growth; however, less lung metastases were detected in mice transplanted with Cdh3-depleted 4T1 cells (Figures 5G and 5H).

In sum, these results indicated that, in both mouse and human breast tumor organoids, leader cells required Cdh3 for their polarization to the leading edge, their capacity to lead directed collective migration, and for efficient metastases *in vivo*.

Figure 3. Cdh3 enrichment identifies a unique leader cell subpopulation

(A–C) Volcano plots of the major K14+ tumor cell subpopulations (#7, no signal; #4, SDF1 gradient; #2, IS flow gradient) relative to all other K14+ tumor cell clusters within each respective sample. Black arrows identify Cdh3 and fold enrichment. Blue arrows identify Cdh1 and fold change.

(D) Venn diagram of overlapping genes in unique K14 tumor cell subpopulations from each experimental setting.

(E–J) Violin plots of Cdh3 expression (E–G) and Cdh1 expression (H–J) in cell clusters for each experimental setting.

(K) IF images of mouse MMTV-PyMT tumor organoid after migration in SDF1 gradient. White arrow direction of migration. Arrowheads identify cells at leading edge that express both K14 and Cdh3.

(L) Pearson's correlation coefficient analysis measuring co-localization of K14 and Cdh3 or K14 and Cdh1 in migrated organoids. For scRNA-seq experiments, n = 3 biological replicates.

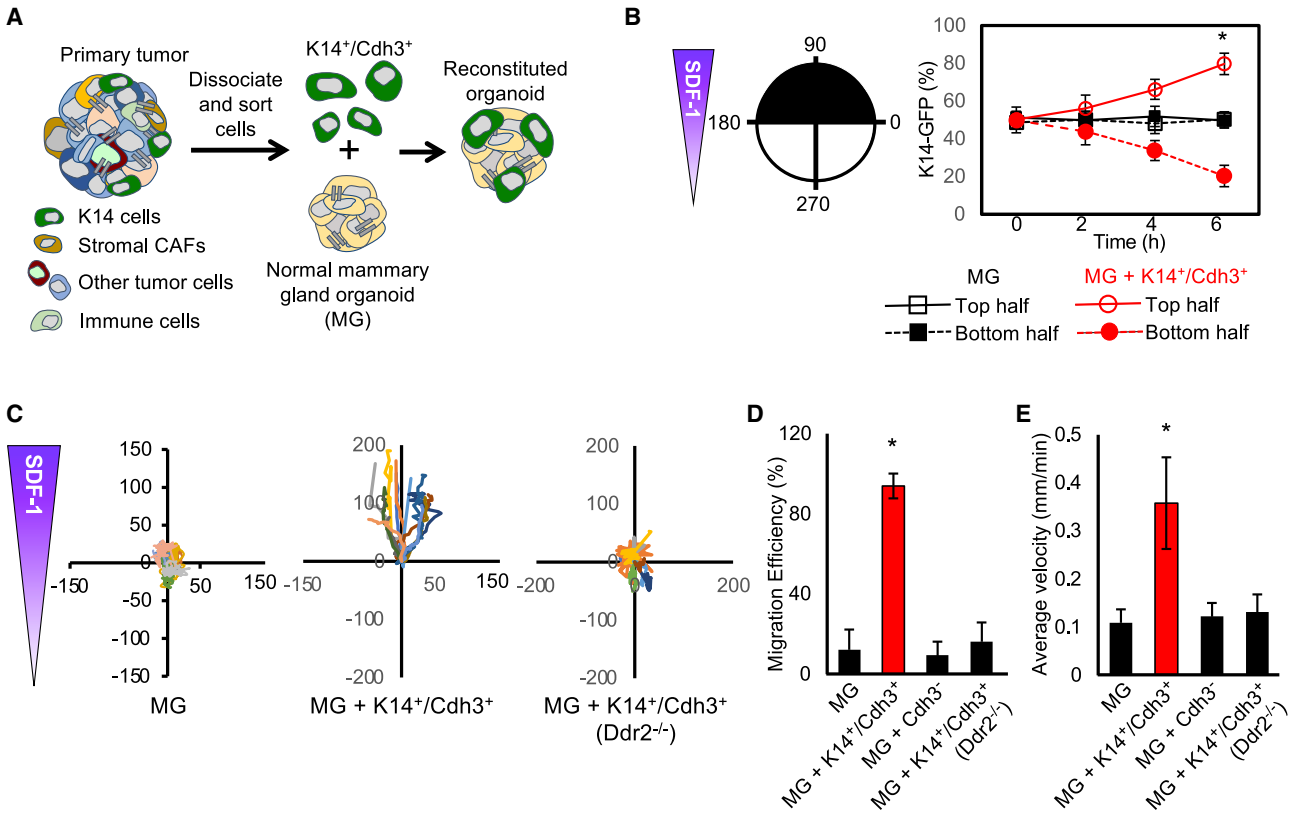

Figure 4. The K14+/Cdh3+ leader cell subpopulation promotes directed collective migration of normal breast organoids

(A) Organoid reconstitution assay: K14+/Cdh3+ cells sorted from MMTV-PyMT tumors, depleted of CD45$^+$ immune cells and CAFs (Thy1+/PDGFRβ+), and mixed with normal mammary gland organoids (MG).

(B) Polarization of K14-Actin.GFP tumor cells in reconstituted organoid.

(C) Migration tracking maps for MGs, K14+/Cdh3+ reconstituted organoids, and K14+/Cdh3+ (Ddr2$^{-/-}$) reconstituted organoids in response to a SDF1.

(D and E) Migration efficiency and velocity for indicated reconstituted organoids. For experiments in microfluidic devices n = 12–15 technical replicates with n = 3 biological replicates were analyzed, *p < 0.05 ANOVA with Tukey's post hoc analysis.

Leader cell polarization and function depend upon Cdh3-dependent protrusion stability and collagen fiber deformation

Computational modeling predicted that high protrusive activity in leader cells is required for directional tumor organoid migration. To test whether Cdh3 was important for leader-cell-protrusive activity, control and Cdh3-depleted mouse PyMT tumor organoids were embedded in 3D collagen-I-containing fluorescent beads and live-cell imaging performed. F-actin was labeled allowing for tracing protrusions along the periphery of the tumor organoids. Control WT tumor organoids stably protruded outward in a given direction (Figure 5I). In contrast, Cdh3-depleted organoids were smaller in size, and their periphery fluctuated back and forth, without stable directionality (Figure 5I). While protrusion area stably increased in WT tumor organoids, it fluctuated with an overall reduction in Cdh3-depleted tumor organoids (Figure 5J). Protrusion efficiency was higher for WT tumor organoids compared with Cdh3-depleted ones (Figure 5K). To test whether effects were specific to leader cells, we isolated K14+; EpCAM+ (leader cells), and K14−; EpCAM+ (follower cells) from mouse PyMT breast tumors and performed similar analyses. Compared with K14− tumor cells, K14+ tumor cells exhibited enhanced protrusions and organoid expansion (Figures S4A, S4B, and S4D). These experiments indicated that Cdh3 expression in K14+ leader tumor cells was important for stable protrusion formation.

Next, we tested whether Cdh3 in leader cells influenced tumor organoid interaction with ECM collagen. We allowed tumor organoids to reside in 3D collagen I with embedded beads over 2 days and imaged bead displacement. Collagen fiber deformation and rates were reduced in Cdh3-depleted tumor organoids (Figures 5L and 5M). K14+ tumor cells, not K14− tumor cells, exhibited enhanced collagen deformation (Figure S4C). Similar changes in protrusion stability and collagen deformation were apparent when human BT549 tumor cell spheroids (±Cdh3) were embedded in 3D collagen I (Figures S4E–S4H).

Cdh3 controls local production of laminin 332 by leader cells at the leading edge

To determine how leader cell interaction(s) with the ECM at the leading edge of migrating collectives generate active adhesions that could reduce the energy barrier imposed by the surrounding collagen fibers (ECM adhesion feedback), we noted that the Cdh3+ subpopulation of K14+ leader cells were enriched for hemi-desmosome receptor genes Col17 and integrin α6β4 as

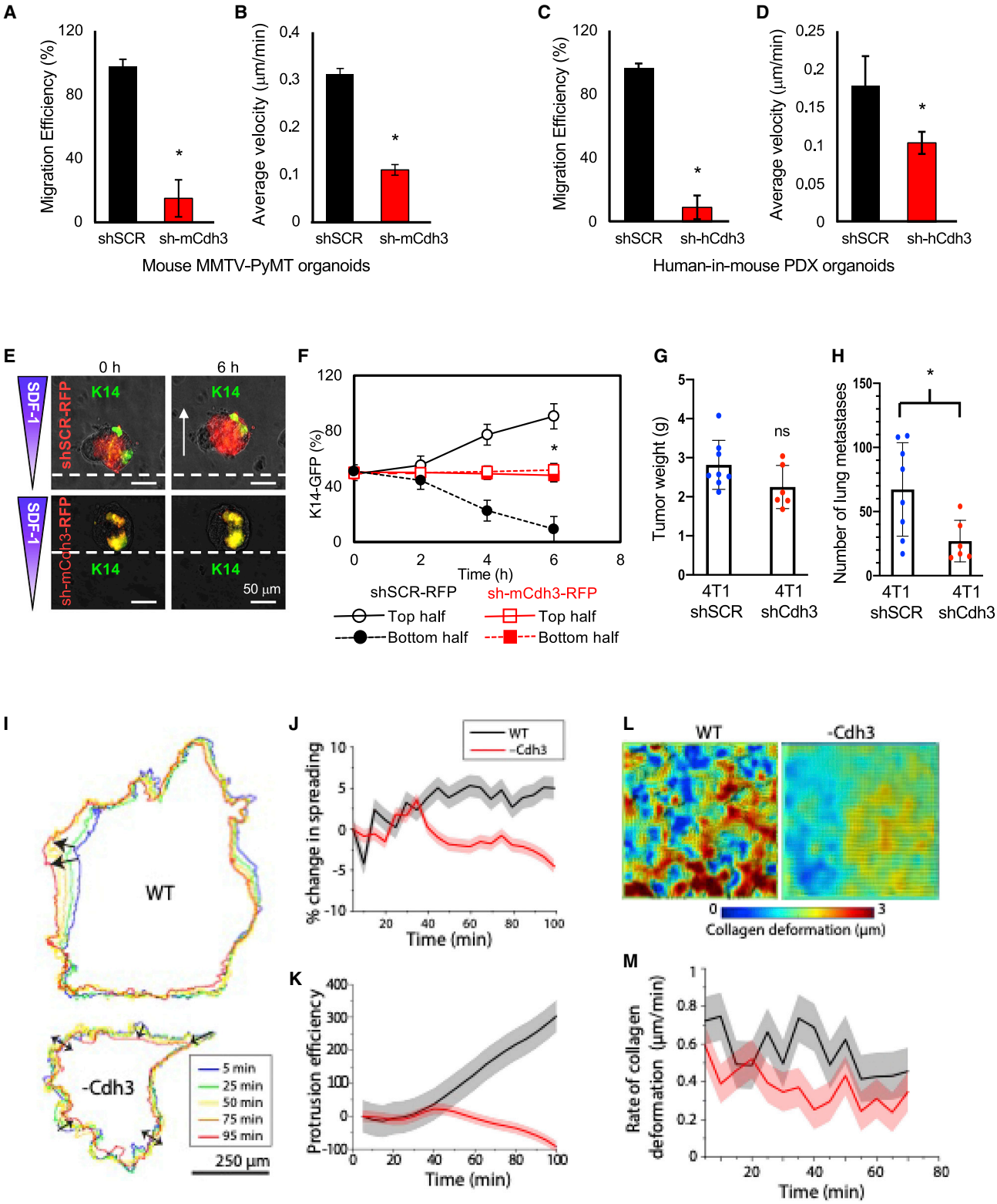

Figure 5. Cdh3 expression in leader cells is required for collective migration, K14 cell polarization, protrusion efficiency, and collagen fiber deformation

(A and B) Migration efficiency and velocity of mouse PyMT breast tumor organoids, ±Cdh3, in a SDF1 gradient.

(C and D) Migration efficiency and velocity of human-in-mouse PDX breast tumor organoids, ±Cdh3, in a SDF1 gradient.

(legend continued on next page)

well as their ligand laminin 332 (Lam332), a basement membrane component (Figures S5A and S5B). Immunostaining of mouse PyMT breast tumor tissue revealed that Lam332 was present at the invasive leading edges, *in vivo* (Figure S5C). Immunostaining of migrating mouse PyMT tumor organoids revealed that Lam332 expression was observed in proximity to K14+ leader cells while collagen 17 (Col17) was present around the entire periphery of the organoids, possibly reflecting proteolytic release of the extracellular domain of Col17[40] (Figure 6A). When Cdh3 was depleted in mouse and human breast tumor organoids expression of Lam332 was, surprisingly, decreased while Col17 expression did not change (Figures 6B, S5D, and S5E, respectively). In orthotopic 4T1 transplant mouse breast tumors, depletion of Cdh3 also resulted in decreased expression of Lam332 at an invasive edge (Figure 6C), confirmed by mRNA analysis (Figure 6D). These results suggested that in leader cells of collectively migrating tumors hemi-desmosomes-Lam332 interactions could contribute to computationally predicted local active adhesions at the leading edge (i.e., ECM adhesion feedback).

To determine if Lam332 expression by leader cells was important for collective migration, we identified two distinct Lamα3 shRNAs lentiviruses: mouse or human. These two shRNA effectively depleted Lam332 (mouse) or Lam5γ2 (human) in breast tumor organoids (Figures S5G and S5H), and mouse 4T1 breast tumor cells (Figure S5I). Depletion of Lamα3 in mouse PyMT breast tumor organoids resulted in decreased directional collective migration (Figures 6E–6G) and inhibited K14+ leader cell polarization (Figure 6H).

Cdh3 controls Lam332 transcription through β-catenin regulation

To determine the molecular pathway(s) whereby Cdh3 regulates Lam332 expression in leader cells we used mouse 4T1 and human BT549 invasive breast tumor cell lines. Both are leader cell "like" in that they express K14+, Cdh3+, Lam332, are protrusive, and invasive *ex vivo* and *in vivo*. In confluent cultures, a situation where cadherin-based cell-cell adhesive contacts are likely to be present, Lam332 protein and mRNA were decreased in 4T1 cells depleted of Cdh3 (Figures S6A and S6B). This suggested that Cdh3-Cdh3-mediated intercellular interactions might regulate Lam332 transcription.

β-catenin is a dual function adhesion/transcriptional co-activator protein.[41] It is recruited to the cytoplasmic tail of cadherin receptors following cell-cell adhesion and can serve as a reservoir of β-catenin in contacted cells. β-catenin also translocates to the nucleus where it can regulate gene transcription in a complex with T-cell factor/lymphoid enhancer factor (TCF) family of DNA-binding proteins. In confluent 4T1 and BT549 cells, depletion of Cdh3 resulted in decreased total cellular β-catenin and decreased nuclear accumulation of β-catenin (Figure 7A; Figure S6C). Pharmacologic inhibition of proteosomes, which degrade cytosolic β-catenin, rescued reduced β-catenin cellular levels in cells lacking Cdh3 (Figure S6D).

Not only do cadherin-cadherin interactions stabilize cellular β-catenin levels but can also potentiate β-catenin signaling.[42] One way is through activation of PI3K/Akt and subsequent inhibition of GSK3β and phosphorylation of β-catenin at S552 that enhances its transcriptional activity.[43] In both cell lines, depletion of Cdh3 resulted in decreased Akt activation and decreased S552 phosphorylation of β-catenin (Figure 7B). Since β-cat S552 phosphorylation enhances its transcriptional activity, we performed chromatin immunoprecipitation (ChIP) experiments to Lam332 genes promoter regions (Table S2) in WT 4T1 cells. Compared with control Ig, both TCF4 and β-catenin ChIP revealed the presence of these protein on the promoter region of all three Lam332 genes (Figure 7C). Positive Sp5 promoter control (Figure S6E).

In sum, these results indicated that Cdh3-Cdh3 intercellular interactions stabilize and activate β-catenin that translocated to the nucleus where it could regulate transcription of Lam332 genes.

Cdh3-Lam332 expression by leader cells regulates integrin activity in leader cells

Protrusion efficiency in migrating cells is a function of integrin-dependent focal adhesion dynamics. Defective protrusion efficiency and collagen deformation in Cdh3-depleted, Lam332-low tumor organoids suggested that integrin function could be altered. When mouse PyMT tumor organoids, ±Lam332, were immunostained with an antibody (9EG7) that recognizes an activated form of β-integrins, there was decreased staining in K14+ leader cells (Figure 7D). In confluent 4T1 and BT549 cells depleted of Cdh3, focal adhesion kinase (FAK), and Src activations were reduced (Figure 7E; Figure S6F). To test whether this could be due to lack of Lam332 production in Cdh3-depleted cells, we added Cdh3-depleted 4T1 cells to Lam332-coated plates. FAK activation was rescued (Figure S6G). We also added WT or Cdh3-depleted mouse PyMT tumor organoids to our microfluidic platform containing a collagen I + Lam332 (1:1) matrix. Defective collective migration of Cdh3-depleted organoids was rescued (Figure 7F). The same result was observed when 4T1 cell aggregates, ±Cdh3, were added to microfluidic devices containing a collagen I: Lam332 matrix (Figures S6H–S6J).

(E and F) Polarization of mouse PyMT K14+ tumor cells, ±Cdh3. (E) Organoids immunostained K14 (green) and lentiviral transduction (red) exposed to a SDF1 gradient. White arrow direction of migration. Broken line start position. (F) Quantification of results in (E) over 6 h.

(G and H) Orthotopic, syngeneic breast transplant experiment. Control 4T1 cells (n = 8) or 4T1 cells depleted of Cdh3 (n = 7). Primary tumor weight (G) and number of lung metastases (H) at termination.

(I) WT and Cdh3-depleted mouse PyMT tumor organoids in 2.3 mg/mL collagen for 12 h, imaging was performed for 1.5 h at 5-min interval. Protrusion outlines of organoids are plotted, visualized by color-coded timestamps. Unidirectional (single arrowheads) and regressive (double arrowheads) protrusions.

(J) Percentage change in tumor organoid area, relative to the reference time point, over time calculated from protrusion outlines.

(K) Protrusion efficiency: area under the curve of percent spreading over time using Y = 0 as baseline.

(L) Spatial heatmap of collagen deformation around tumor organoids.

(M) Rate of collagen deformation by tumor organoids over time. n = 3 for WT and n = 5 for Cdh3− depleted. Solid lines mean and shaded background standard error (SE). For experiments in microfluidic devices n = 12–15 technical replicates with n = 3 biological replicates were analyzed. For all experiments, *p < 0.05 ANOVA with Tukey's post hoc analysis.

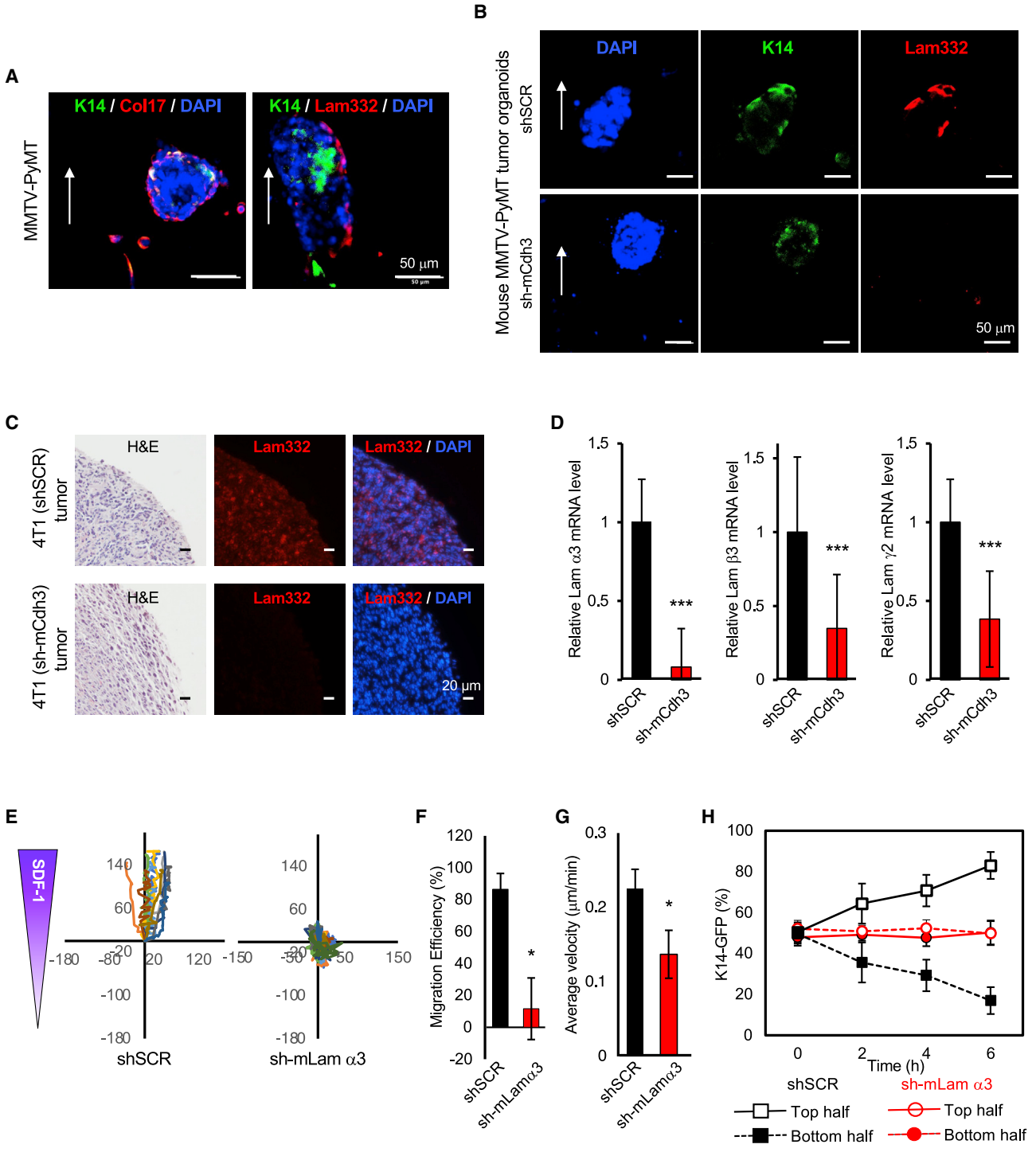

Figure 6. Cdh3 controls Lam332 expression in leader cells

(A) IF images of WT PyMT tumor organoids migrating in a SDF1 gradient (white arrow), stained for indicated proteins.

(B) IF images of PyMT tumor organoids, ±Cdh3, migrated in a SDF1 chemical gradient (white arrow) stained for indicated proteins.

(C) H&E and IF images of the invasive edge of 4T1 breast primary tumor sections, ±Cdh3, stained for indicated proteins.

(D) qPCR analysis of Lam332 genes mRNA levels in 4T1 breast tumors, ±Cdh3.

(E) Migration tracking maps for PyMT tumor organoids, ±Lamα3, in a SDF1 gradient.

(F and G) Migration efficiency and velocity of organoids in (E).

(H) Polarization of K14+ tumor leader cells in mouse tumor organoids, ±Lamα3. For experiments in microfluidic devices n = 12–15 technical replicates with n = 3 biological replicates were analyzed. For all experiments, *p < 0.05, ***p < 0.01 ANOVA with Tukey's post hoc analysis.

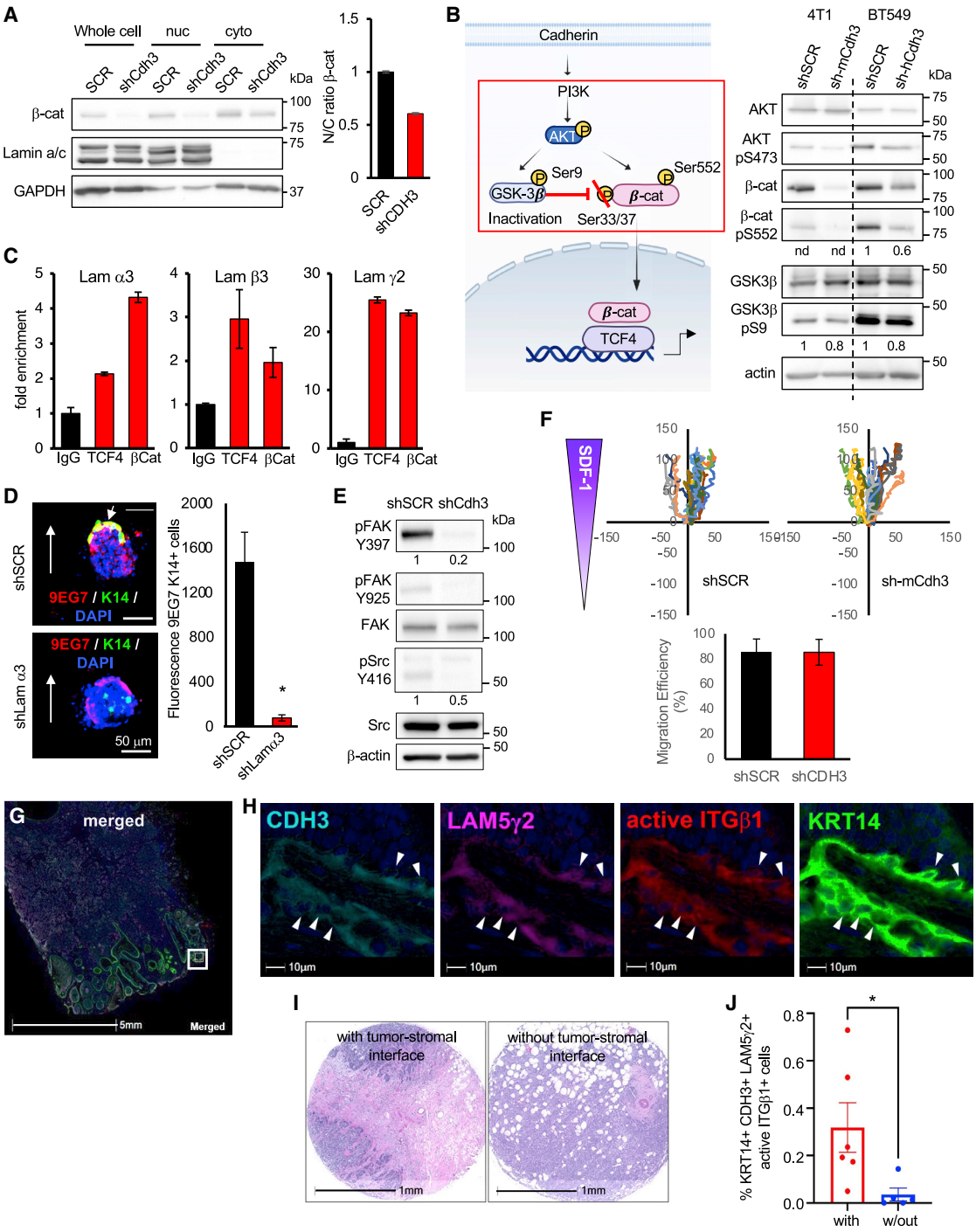

Figure 7. Cdh3 controls β-catenin activity to stimulate local laminin 332 production that is required for collective migration

(A) Subcellular fractionation and quantitative western blots of confluent mouse 4T1 cells, ±Cdh3. Nuclear/cytoplasmic ratio of β-catenin levels was determined by comparing subcellular extract levels normalized to equivalent number of cells.

(B) Quantitative western blot analyses of confluent mouse 4T1 and human BT549 cells, ±Cdh3, with indicated antibodies. β-cat-pS552 in 4T1 cells not determined (nd) as total β-cat in Cdh3-depleted cells was too low. Cartoon on left highlights signaling pathways interrogated.

(C) Chromatin IP of confluent WT mouse 4T1 cells with indicated antibodies and PCR of promoter regions of Lam332 genes.

(D) IF images of PyMT breast tumor organoids, ±Lamα3, exposed to a SDF1 gradient (arrow) and stained for K14-Actin.GFP (green) and active β-integrin (9EG7) (red). Arrowheads identify co-stained cells at leading edge. 9EG7 fluorescence in K14+ cells quantified (right).

(E) Western blot of confluent mouse 4T1 cells, ±Cdh3, with indicated antibodies.

(F) Migration tracking maps and migration efficiency of PyMT tumor organoids, ±Cdh3, in microfluidic devices containing collagen I: laminin 332 (1:1) and exposed to a SDF1 gradient.

(legend continued on next page)

Depletion of Cdh3 in breast cancer cell lines can decrease adhesion to a laminin matrix, due to decreased expression of the laminin receptor integrin α6β4.[44] Depletion of Cdh3 did not affect cell surface integrin β1 or α6 in BT549 (Figure S7). As BT549 cells did not express integrin β4 (Figure S7), we performed western blots of 4T1 cells (±Cdh3). There was no change in the level of β4 integrin when Cdh3 was depleted (Figure S7). These results, along with the rescue of Cdh3-depleted primary tumor organoid migration by addition of exogenous Lam332, suggested that integrin laminin receptor expression was not affected by depletion of Cdh3.

Our combined data in mouse and human breast tumor cells and organoids suggested a model whereby Cdh3 signaling via β-catenin controls transcription and production of Lam332 by leader cells at the leading edge. This locally secreted Lam332 activates integrins in leader cells to support functional protrusions that sustain collective migration. If correct, then K14, Cdh3, laminin, and activated integrin expression should co-localize to cells at the invasive leading edge of breast tumors. We performed multiplex immunohistochemical analysis on a human breast tumor microarray (TMA) from untreated women with metastatic disease (Figures 7G–7J). Breast tumor biopsies taken from the center of tumors may have little tumor-stromal boundaries. We selected 6 TMA samples with significant tumor-stromal interface and contrasted these with 6 samples without tumor-stromal interfaces (see Figure 7I). Samples were sequentially stained with antibodies to CDH3, laminin 5γ2, active ITGβ1, and KRT14, and images were quantified using image analysis platform (HALO software). All proteins co-localized to the same set of cells at the leading, invasive edge (Figures 7G and 7H). Samples with tumor-stromal interfaces had increased co-localization compared with samples without tumor-stromal interfaces. The small percentage of co-stained cells likely reflects the few KRT14+ leader cells present in tumors.

DISCUSSION

Although there has been significant progress toward understanding molecular and functional heterogeneity of tumor cells[45,46] and associated stromal cells,[33] leader cell heterogeneity has not been addressed, particularly in primary tumors. The Cdh3+ subpopulation of K14+ leader cells was also enriched for other cell surface signaling receptors, such as Fgfr2, Jag1, Jag2, CNTFR, that have been associated with tumor progression and metastases.[47–50] Epithelial mesenchymal transition (EMT) inducing transcription factors are also implicated in controlling breast tumor invasion and metastasis. Of the major tumor EMT transcriptional regulators (e.g., Snail, Twist, Zeb, and Prrx) only Snail2 was enriched in the Cdh3+ leader cell subpopulation. Snail2 enrichment is particularly interesting as it has been shown to transcriptionally activate expression of Cdh3 and requires Cdh3 for its EMT actions.[51] This could explain the restricted expression of Cdh3 in breast tumor leader cells.

Cadherin-mediated cell-cell interactions between follower cells, leader cells, leader-follower cells, as well as CAFs and leader cells are central to collective cell migration.[52,53] In tumors dynamic expression of Cdh1 has received most attention but epithelial tumor cells can switch from expressing Cdh1 to Cdh3.[54,55] High Cdh3 expression in patients with a variety of cancers, including invasive TNBC breast cancers, correlate with poor prognosis.[37,54,56,57] Cdh3 is also expressed by normal basal breast epithelial cells.[55] Finally, developmental genetic defects are associated with loss of Cdh3 and these have been linked to altered cell-cell and cell-matrix interactions.[55]

Cdh1 expression in the K14+/Cdh3+ subpopulation was low, and in response to migratory signals, its level was unaffected. Rather, Cdh1 was predominantly expressed by follower (K14−) tumor cells. Some models of collective migration suggest leader-follower cell boundaries consist of heterotypic Cdh1-Cdh3 junctions.[52] Whether this interaction explains the computationally hypothesized requirement for an intermediate adhesion strength between leader-followers remains to be determined. Regardless, a key result of our modeling effort was the prediction that relative strengths of any combination of leader-follower cell adhesions alone did not capture leader cell behavior and function during collective tumor organoid migration. Rather, the two most important variables for effective collective migration were leader cell preferential protrusions and, at least, a subpopulation of leader cells that form active ECM adhesions upon arriving at the invasive front to reduce initial resistance presented by ECM collagen. We find that Cdh3+/K14+ leader cells, as opposed to K14− tumor cells, exhibit enhanced Cdh3-dependent protrusive activity.

When leader cells arrive at the leading edge, they need to overcome resistance to continued movement presented by the ECM. One way it appears they do so is by locally secreting the basement membrane protein Lam332. Cdh3 is required for this localized Lam332 production. This localized signal likely sustains leader-cell-protrusive forces that could be transmitted to follower cells according to force equilibrium (ECM feedback). When follower tumor cells engage with ECM, this signal and feedback does not appear to arise. This active feedback could arise from alignment of collagen, degradation of collagen, or increased forces in leader cells due to integrin-based signaling, or a combination thereof. Our computational model used energy-based criterion to implement this active feedback, which does not distinguish among these possibilities. However, experimentally Cdh3-Cdh3 interactions in leader cells at the leading edge controlled local production of laminin by activating β-catenin/TCF4 nuclear complexes that induce transcription of Lam332 genes. Local laminin production was required for efficient integrin/FA mediated protrusions in leader cells. Previously, β-catenin has been shown to regulate the transcription of the laminin γ2 gene in human colon cancer cell lines.[58]

Cadherin-based cell-cell adhesion can stimulate cell-ECM adhesions and traction force,[59,60] but the mechanism is not fully

(G–J) Multiplex immunohistochemical analysis of human breast tumor TMAs from untreated patients with metastatic disease. (G) Low resolution merged image stained with indicated antibodies. Samples with tumor-stromal interfaces were scored and compared with equal number without tumor-stromal interface (I and J). n = 6 for each. (H) Higher magnification images delineated by the white box in (G). Arrowheads in each panel identify the same cells. For experiments in microfluidic devices n = 12–15 technical replicates with n = 3 biological replicates were analyzed. For all experiments, *p < 0.05 ANOVA with Tukey's post hoc analysis.

understood. With respect to Cdh3, overexpression in cell lines can induce secretion of Decorin. which modifies collagen fiber organization and alignment.[61] This altered collagen structure activates integrin, and Decorin was required for Cdh3-induced collective migration. Thus, in that setting Cdh3 indirectly stimulates collagen deformation. Our scRNA-seq analysis revealed that Cdh3+ leader cells do not express Decorin. Rather, Decorin was expressed by organoid-associated CAFs. Whether CAF produced Decorin contributes to tumor organoid collective migration remains to be determined.

Perhaps hemi-desmosome function in leader cells contributes to collagen fiber deformation. Hemi-desmosomes are cell-matrix adhesive structures associated with the keratin cytoskeleton. In skin, they anchor the basal layer of epithelial cells to the basement membrane through an association with Lam332.[62] The hemi-desmosome intermediate filament association enables cells to withstand mechanical stress and tension,[63] yet can also modulate cellular mechanical force through intracellular crosstalk with FAs.[64] In keratinocytes loss of hemi-desmosomes resulted in increased traction force generation. However, in breast tumor organoids, loss of Cdh3 and Lam332 resulted in decreased collagen fiber deformation rate. This could reflect the fact that hemi-desmosome function can be cell and context dependent, as deletion of Plectin (cytosolic adapter of hemi-desmosomes) in myoblasts or fibroblasts results in decreased traction forces.[65,66] Although the subpopulation of leader cells was enriched for expression of hemi-desmosome components, in the context of an invasive tumor perhaps they behave in a more mesenchymal manner as evident by enriched expression of Snail2 and Cdh3.

Further understanding of the molecular and functional characteristics of leader cell heterogeneity and their role in collective migration of tumors could lead to the identification of potential therapeutic targets that may prevent and or treat breast tumor progression and metastatic disease.

Limitations of the study

Our computational models focused on functions of leader and follower cell populations and their respective interactions with surrounding collagen. Although this model identified specific properties of leader cells, there are several limitations and approximations that were necessary for computational optimization. In future work, to better capture tumor heterogeneity, we can include other cell types (e.g., CAFs) that could contribute to adhesive and protrusive properties. Currently, the surrounding ECM is modeled as a field, which could be composed of fibers of tunable density and crosslinking that could be aligned or degraded, as occurs *in vivo*. These modifications may generate new hypotheses around different roles of cell-ECM interactions in tumor organoid migration.

While we have generated data supporting a Cdh3—β-catenin—laminin signaling pathway controlling breast tumor collective migration, we have not formally demonstrated active β-catenin signaling in Cdh3+ leader cells *in vivo*. Wnt/β-catenin is known to regulate leader cell functions during collective migration of the zebrafish lateral line primordium.[67] There are highly sensitive β-catenin reporter mice[68] that could be used in breast tumor models to determine if β-catenin is active in leader cells *in vivo*.

STAR★METHODS

Detailed methods are provided in the online version of this paper and include the following:

- KEY RESOURCES TABLE
- RESOURCE AVAILABILITY
  - Lead contact
  - Materials availability
  - Data and code availability
- EXPERIMENTAL MODEL AND SUBJECT DETAILS
  - Mouse Breast Tumor Models
  - Breast tumor cell lines
- METHOD DETAILS
  - Computational model
  - Calibrating cell-cell adhesions in Potts modeling
  - Primary breast tumor organoid isolation and culture
  - Primary breast organoid reconstitution assay
  - Single cell RNA sequencing (scRNAseq) and analysis
  - shRNA lentiviral depletion of gene expression
  - Transwell Invasion Assay
  - 3D Cell Invasion Assay
  - Live-cell imaging and analysis
  - Immunofluorescence of breast tumor organoids
  - Gene expression
  - Protein expression
  - Subcellular fractionation
  - Chromatin immunoprecipitation (ChIP) Assay
  - Multiplex immunohistochemistry
- QUANTIFICATION AND STATISTICAL ANALYSIS

SUPPLEMENTAL INFORMATION

Supplemental information can be found online at https://doi.org/10.1016/j.devcel.2022.12.005.

ACKNOWLEDGMENTS

This work was supported by the following funding mechanisms: R01CA223758 and U54CA210173 (G.D.L.), R35GM128764 (A.P.), NSF Center for Engineering MechanoBiology (A.P.), American Cancer Society Postdoctoral Fellowship (PF-17-238-01-CSM) (P.Y.H.). A Centene Corporation contract (P19-00559) for the Washington University-Centene ARCH Personalized Medicine Initiative (G.D.L.). We thank the following people: Ashley C. King, Caleb McCurdy, and Jessanne Y. Lichtenberg for assistance synthesizing the microfluidic systems, Takako Sasaki for the laminin α3 antibody (1110+), Prabhakar Andhey and Maxim Artyomov for bioinformatic assistance, the Washington University Center for Cellular Imaging (WUCCI) and VCU Nanomaterials Core Characterization Facility for imaging assistance, the Flow cytometry and fluorescence-activated cell sorting Core at Washington University, and the McDonnell Genome Institute at Washington University for single-cell sequencing. We would like to thank Cara Gottardi, Northwestern University for assistance in design of β-cat/TCF ChIP experiments. We support inclusive, diverse, and equitable conduct of research.

AUTHOR CONTRIBUTIONS

P.Y.H., G.D.L., and A.P. conceived the project, designed experiments, and wrote the manuscript. P.Y.H., D.C., Y.C., M.C., J.Y., S.A.S., V.M., and J.A. performed experiments and, or data analysis. J.M. and A.P. performed computational modeling and wrote corresponding results.

DECLARATION OF INTERESTS

The Longmore laboratory receives funding from Pfizer-CTI, San Diego CA and Centene Corporation, St. Louis, MO, USA.

Received: November 23, 2021
Revised: August 10, 2022
Accepted: December 7, 2022
Published: January 9, 2023

REFERENCES

1. Shellard, A., and Mayor, R. (2020). Rules of collective migration: from the wildebeest to the neural crest. Philos. Trans. R. Soc. Lond. B Biol. Sci. *375*, 20190387. https://doi.org/10.1098/rstb.2019.0387.
2. Capuana, L., Boström, A., and Etienne-Manneville, S. (2020). Multicellular scale front-to-rear polarity in collective migration. Curr. Opin. Cell Biol. *62*, 114–122. https://doi.org/10.1016/j.ceb.2019.10.001.
3. Shellard, A., and Mayor, R. (2020). All roads lead to directional cell migration. Trends Cell Biol. *30*, 852–868. https://doi.org/10.1016/j.tcb.2020.08.002.
4. Aceto, N., Toner, M., Maheswaran, S., and Haber, D.A. (2015). En route to metastasis: circulating tumor cell clusters and epithelial-to-mesenchymal transition. Trends Cancer *1*, 44–52. https://doi.org/10.1016/j.trecan.2015.07.006.
5. Friedl, P., and Gilmour, D. (2009). Collective cell migration in morphogenesis, regeneration and cancer. Nat. Rev. Mol. Cell Biol. *10*, 445–457. https://doi.org/10.1038/nrm2720.
6. Etienne-Manneville, S. (2014). Neighborly relations during collective migration. Curr. Opin. Cell Biol. *30*, 51–59. https://doi.org/10.1016/j.ceb.2014.06.004.
7. van Helvert, S., Storm, C., and Friedl, P. (2018). Mechanoreciprocity in cell migration. Nat. Cell Biol. *20*, 8–20. https://doi.org/10.1038/s41556-017-0012-0.
8. Aceto, N., Bardia, A., Miyamoto, D.T., Donaldson, M.C., Wittner, B.S., Spencer, J.A., Yu, M., Pely, A., Engstrom, A., Zhu, H., et al. (2014). Circulating tumor cell clusters are oligoclonal precursors of breast cancer metastasis. Cell *158*, 1110–1122. https://doi.org/10.1016/j.cell.2014.07.013.
9. Bulfoni, M., Turetta, M., Del Ben, F., Di Loreto, C., Beltrami, A.P., and Cesselli, D. (2016). Dissecting the heterogeneity of circulating tumor cells in metastatic breast cancer: going far beyond the needle in the haystack. Int. J. Mol. Sci. *17*, 1775. https://doi.org/10.3390/ijms17101775.
10. Au, S.H., Storey, B.D., Moore, J.C., Tang, Q., Chen, Y.L., Javaid, S., Sarioglu, A.F., Sullivan, R., Madden, M.W., O'Keefe, R., et al. (2016). Clusters of circulating tumor cells traverse capillary-sized vessels. Proc. Natl. Acad. Sci. USA *113*, 4947–4952. https://doi.org/10.1073/pnas.1524448113.
11. Allen, T.A., Asad, D., Amu, E., Hensley, M.T., Cores, J., Vandergriff, A., Tang, J., Dinh, P.U., Shen, D., Qiao, L., et al. (2019). Circulating tumor cells exit circulation while maintaining multicellularity, augmenting metastatic potential. J. Cell Sci. *132*, jcs231563. https://doi.org/10.1242/jcs.231563.
12. Brouwer, A., De Laere, B., Peeters, D., Peeters, M., Salgado, R., Dirix, L., and Van Laere, S. (2016). Evaluation and consequences of heterogeneity in the circulating tumor cell compartment. Oncotarget *7*, 48625–48643. https://doi.org/10.18632/oncotarget.8015.
13. Miyamoto, D.T., Ting, D.T., Toner, M., Maheswaran, S., and Haber, D.A. (2016). Single-cell analysis of circulating tumor cells as a window into tumor heterogeneity. Cold Spring Harbor Symp. Quant. Biol. *81*, 269–274. https://doi.org/10.1101/sqb.2016.81.031120.
14. Turashvili, G., and Brogi, E. (2017). Tumor heterogeneity in breast cancer. Front. Med. (Lausanne) *4*, 227. https://doi.org/10.3389/fmed.2017.00227.
15. Lawson, D.A., Kessenbrock, K., Davis, R.T., Pervolarakis, N., and Werb, Z. (2018). Tumour heterogeneity and metastasis at single-cell resolution. Nat. Cell Biol. *20*, 1349–1360. https://doi.org/10.1038/s41556-018-0236-7.
16. Toullec, A., Gerald, D., Despouy, G., Bourachot, B., Cardon, M., Lefort, S., Richardson, M., Rigaill, G., Parrini, M.C., Lucchesi, C., et al. (2010). Oxidative stress promotes myofibroblast differentiation and tumour spreading. EMBO Mol. Med. *2*, 211–230. https://doi.org/10.1002/emmm.201000073.
17. Benyahia, Z., Dussault, N., Cayol, M., Sigaud, R., Berenguer-Daizé, C., Delfino, C., Tounsi, A., Garcia, S., Martin, P.M., Mabrouk, K., and Ouafik, L. (2017). Stromal fibroblasts present in breast carcinomas promote tumor growth and angiogenesis through adrenomedullin secretion. Oncotarget *8*, 15744–15762. https://doi.org/10.18632/oncotarget.14999.
18. Ewald, A.J., Brenot, A., Duong, M., Chan, B.S., and Werb, Z. (2008). Collective epithelial migration and cell rearrangements drive mammary branching morphogenesis. Dev. Cell *14*, 570–581. https://doi.org/10.1016/j.devcel.2008.03.003.
19. Khalil, A.A., and Friedl, P. (2010). Determinants of leader cells in collective cell migration. Integr. Biol. (Camb) *2*, 568–574. https://doi.org/10.1039/c0ib00052c.
20. Mayor, R., and Etienne-Manneville, S. (2016). The front and rear of collective cell migration. Nat. Rev. Mol. Cell Biol. *17*, 97–109. https://doi.org/10.1038/nrm.2015.14.
21. Chen, B.J., Tang, Y.J., Tang, Y.L., and Liang, X.H. (2019). What makes cells move: requirements and obstacles for leader cells in collective invasion. Exp. Cell Res. *382*, 111481. https://doi.org/10.1016/j.yexcr.2019.06.026.
22. Vishwakarma, M., Di Russo, J., Probst, D., Schwarz, U.S., Das, T., and Spatz, J.P. (2018). Mechanical interactions among followers determine the emergence of leaders in migrating epithelial cell collectives. Nat. Commun. *9*, 3469. https://doi.org/10.1038/s41467-018-05927-6.
23. Nguyen-Ngoc, K.-V., Cheung, K.J., Brenot, A., Shamir, E.R., Gray, R.S., Hines, W.C., Yaswen, P., Werb, Z., and Ewald, A.J. (2012). ECM microenvironment regulates collective migration and local dissemination in normal and malignant mammary epithelium. Proc. Natl. Acad. Sci. USA *109*, E2595–E2604. https://doi.org/10.1073/pnas.1212834109.
24. Cheung, K.J., Padmanaban, V., Silvestri, V., Schipper, K., Cohen, J.D., Fairchild, A.N., Gorin, M.A., Verdone, J.E., Pienta, K.J., Bader, J.S., and Ewald, A.J. (2016). Polyclonal breast cancer metastases arise from collective dissemination of keratin 14-expressing tumor cell clusters. Proc. Natl. Acad. Sci. USA *113*, E854–E863. https://doi.org/10.1073/pnas.1508541113.
25. Cheung, K.J., Gabrielson, E., Werb, Z., and Ewald, A.J. (2013). Collective invasion in breast cancer requires a conserved basal epithelial program. Cell *155*, 1639–1651. https://doi.org/10.1016/j.cell.2013.11.029.
26. Cheung, K.J., and Ewald, A.J. (2016). A collective route to metastasis: seeding by tumor cell clusters. Science *352*, 167–169. https://doi.org/10.1126/science.aaf6546.
27. Theveneau, E., and Linker, C. (2017). Leaders in collective migration: are front cells really endowed with a particular set of skills? F1000Res *6*, 1899. https://doi.org/10.12688/f1000research.11889.1.
28. Hwang, P.Y., Brenot, A., King, A.C., Longmore, G.D., and George, S.C. (2019). Randomly distributed K14+ Breast Tumor Cells Polarize to the Leading Edge and Guide Collective Migration in Response to Chemical and Mechanical Environmental Cues. Cancer Res. *79*, 1899–1912. https://doi.org/10.1158/0008-5472.CAN-18-2828.
29. Katt, M.E., Placone, A.L., Wong, A.D., Xu, Z.S., and Searson, P.C. (2016). In vitro tumor models: advantages, disadvantages, variables, and selecting the right platform. Front. Bioeng. Biotechnol. *4*, 12. https://doi.org/10.3389/fbioe.2016.00012.
30. Weber, C.E., and Kuo, P.C. (2012). The tumor microenvironment. Surg. Oncol. *21*, 172–177. https://doi.org/10.1016/j.suronc.2011.09.001.
31. Clark, A.G., and Vignjevic, D.M. (2015). Modes of cancer cell invasion and the role of the microenvironment. Curr. Opin. Cell Biol. *36*, 13–22. https://doi.org/10.1016/j.ceb.2015.06.004.
32. Emon, B., Bauer, J., Jain, Y., Jung, B., and Saif, T. (2018). Biophysics of tumor microenvironment and cancer metastasis - A mini review. Comp. Struct. Biotechnol. J. *16*, 279–287. https://doi.org/10.1016/j.csbj.2018.07.003.

33. Bartoschek, M., Oskolkov, N., Bocci, M., Lövrot, J., Larsson, C., Sommarin, M., Madsen, C.D., Lindgren, D., Pekar, G., Karlsson, G., et al. (2018). Spatially and functionally distinct subclasses of breast cancer-associated fibroblasts revealed by single cell RNA sequencing. Nat. Commun. *9*, 5150. https://doi.org/10.1038/s41467-018-07582-3.

34. van Roy, F. (2014). Beyond E-cadherin: roles of other cadherin superfamily members in cancer. Nat. Rev. Cancer *14*, 121–134. https://doi.org/10.1038/nrc3647.

35. Padmanaban, V., Krol, I., Suhail, Y., Szczerba, B.M., Aceto, N., Bader, J.S., and Ewald, A.J. (2019). E-cadherin is required for metastasis in multiple models of breast cancer. Nature *573*, 439–444. https://doi.org/10.1038/s41586-019-1526-3.

36. Corsa, C.A., Brenot, A., Grither, W.R., Van Hove, S., Loza, A.J., Zhang, K., Ponik, S.M., Liu, Y., DeNardo, D.G., Eliceiri, K.W., et al. (2016). The action of discoidin domain Receptor 2 in basal tumor cells and stromal cancer-associated fibroblasts is critical for breast cancer metastasis. Cell Rep. *15*, 2510–2523. https://doi.org/10.1016/j.celrep.2016.05.033.

37. Sridhar, S., Rajesh, C., Jishnu, P.V., Jayaram, P., and Kabekkodu, S.P. (2020). Increased expression of P-cadherin is an indicator of poor prognosis in breast cancer: a systematic review and meta-analysis. Breast Cancer Res. Treat. *179*, 301–313. https://doi.org/10.1007/s10549-019-05477-5.

38. Vieira, A.F., Dionísio, M.R., Gomes, M., Cameselle-Teijeiro, J.F., Lacerda, M., Amendoeira, I., Schmitt, F., and Paredes, J. (2017). P-cadherin: a useful biomarker for axillary-based breast cancer decisions in the clinical practice. Mod. Pathol. *30*, 698–709. https://doi.org/10.1038/modpathol.2016.232.

39. Plutoni, C., Bazellieres, E., Le Borgne-Rochet, M., Comunale, F., Brugues, A., Séveno, M., Planchon, D., Thuault, S., Morin, N., Bodin, S., et al. (2016). P-cadherin promotes collective cell migration via a Cdc42-mediated increase in mechanical forces. J. Cell Biol. *212*, 199–217. https://doi.org/10.1083/jcb.201505105.

40. Franzke, C.W., Tasanen, K., Schäcke, H., Zhou, Z., Tryggvason, K., Mauch, C., Zigrino, P., Sunnarborg, S., Lee, D.C., Fahrenholz, F., et al. (2002). Transmembrane collagen XVII, an epithelial adhesion protein, is shed from the cell surface by ADAMs. EMBO J. *21*, 5026–5035. https://doi.org/10.1093/emboj/cdf532.

41. McCrea, P.D., Maher, M.T., and Gottardi, C.J. (2015). Nuclear signaling from cadherin adhesion complexes. Curr. Top. Dev. Biol. *112*, 129–196. https://doi.org/10.1016/bs.ctdb.2014.11.018.

42. Zhang, J., Woodhead, G.J., Swaminathan, S.K., Noles, S.R., McQuinn, E.R., Pisarek, A.J., Stocker, A.M., Mutch, C.A., Funatsu, N., and Chenn, A. (2010). Cortical neural precursors inhibit their own differentiation via N-cadherin maintenance of beta-catenin signaling. Dev. Cell *18*, 472–479. https://doi.org/10.1016/j.devcel.2009.12.025.

43. Fang, D., Hawke, D., Zheng, Y., Xia, Y., Meisenhelder, J., Nika, H., Mills, G.B., Kobayashi, R., Hunter, T., and Lu, Z. (2007). Phosphorylation of beta-catenin by AKT promotes beta-catenin transcriptional activity. J. Biol. Chem. *282*, 11221–11229. https://doi.org/10.1074/jbc.M611871200.

44. Vieira, A.F., Ribeiro, A.S., Dionísio, M.R., Sousa, B., Nobre, A.R., Albergaria, A., Santiago-Gómez, A., Mendes, N., Gerhard, R., Schmitt, F., et al. (2014). P-cadherin signals through the laminin receptor $\alpha 6\beta 4$ integrin to induce stem cell and invasive properties in basal-like breast cancer cells. Oncotarget *5*, 679–692. https://doi.org/10.18632/oncotarget.1459.

45. Qian, M., Wang, D.C., Chen, H., and Cheng, Y. (2017). Detection of single cell heterogeneity in cancer. Semin. Cell Dev. Biol. *64*, 143–149. https://doi.org/10.1016/j.semcdb.2016.09.003.

46. Shen, Y., Schmidt, B.U.S., Kubitschke, H., Morawetz, E.W., Wolf, B., Käs, J.A., and Losert, W. (2020). Detecting heterogeneity in and between breast cancer cell lines. Cancer Converg. *4*, 1. https://doi.org/10.1186/s41236-020-0010-1.

47. Pearson, A., Smyth, E., Babina, I.S., Herrera-Abreu, M.T., Tarazona, N., Peckitt, C., Kilgour, E., Smith, N.R., Geh, C., Rooney, C., et al. (2016). High-level clonal FGFR amplification and response to FGFR inhibition in a translational clinical trial. Cancer Discov. *6*, 838–851. https://doi.org/10.1158/2159-8290.CD-15-1246.

48. Sethi, N., Dai, X., Winter, C.G., and Kang, Y. (2011). Tumor-derived JAGGED1 promotes osteolytic bone metastasis of breast cancer by engaging notch signaling in bone cells. Cancer Cell *19*, 192–205. https://doi.org/10.1016/j.ccr.2010.12.022.

49. Bednarz-Knoll, N., Efstathiou, A., Gotzhein, F., Wikman, H., Mueller, V., Kang, Y., and Pantel, K. (2016). Potential involvement of Jagged1 in metastatic progression of human breast carcinomas. Clin. Chem. *62*, 378–386. https://doi.org/10.1373/clinchem.2015.246686.

50. Xing, F., Okuda, H., Watabe, M., Kobayashi, A., Pai, S.K., Liu, W., Pandey, P.R., Fukuda, K., Hirota, S., Sugai, T., et al. (2011). Hypoxia-induced Jagged2 promotes breast cancer metastasis and self-renewal of cancer stem-like cells. Oncogene *30*, 4075–4086. https://doi.org/10.1038/onc.2011.122.

51. Idoux-Gillet, Y., Nassour, M., Lakis, E., Bonini, F., Theillet, C., Du Manoir, S., and Savagner, P. (2018). Slug/Pcad pathway controls epithelial cell dynamics in mammary gland and breast carcinoma. Oncogene *37*, 578–588. https://doi.org/10.1038/onc.2017.355.

52. Khalil, A.A., and de Rooij, J. (2019). Cadherin mechanotransduction in leader-follower cell specification during collective migration. Exp. Cell Res. *376*, 86–91. https://doi.org/10.1016/j.yexcr.2019.01.006.

53. Labernadie, A., Kato, T., Brugués, A., Serra-Picamal, X., Derzsi, S., Arwert, E., Weston, A., González-Tarragó, V., Elosegui-Artola, A., Albertazzi, L., et al. (2017). A mechanically active heterotypic E-cadherin/N-cadherin adhesion enables fibroblasts to drive cancer cell invasion. Nat. Cell Biol. *19*, 224–237. https://doi.org/10.1038/ncb3478.

54. Christgen, M., Bartels, S., van Luttikhuizen, J.L., Bublitz, J., Rieger, L.U., Christgen, H., Stark, H., Sander, B., Lehmann, U., Steinemann, D., et al. (2020). E-cadherin to P-cadherin switching in lobular breast cancer with tubular elements. Mod. Pathol. *33*, 2483–2498. https://doi.org/10.1038/s41379-020-0591-3.

55. Albergaria, A., Ribeiro, A.-S., Vieira, A.-F., Sousa, B., Nobre, A.-R., Seruca, R., Schmitt, F., and Paredes, J. (2011). P-cadherin role in normal breast development and cancer. Int. J. Dev. Biol. *55*, 811–822. https://doi.org/10.1387/ijdb.113382aa.

56. Imai, S., Kobayashi, M., Takasaki, C., Ishibashi, H., and Okubo, K. (2018). High expression of P-cadherin is significantly associated with poor prognosis in patients with non-small-cell lung cancer. Lung Cancer *118*, 13–19. https://doi.org/10.1016/j.lungcan.2018.01.018.

57. Li, B., Gong, D., Wang, F., and Wan, X. (2019). P-cadherin promotes cervical cancer growth and invasion through affecting the expression of E-cadherin and p120 catenin. EJGO *40*, 224–231. https://doi.org/10.12892/ejgo4374.2019.

58. Hlubek, F., Jung, A., Kotzor, N., Kirchner, T., and Brabletz, T. (2001). Expression of the Invasion Factor laminin $\gamma 2$ in Colorectal Carcinomas Is Regulated by β-Catenin1. Cancer Res. *61*, 8089–8093.

59. Jasaitis, A., Estevez, M., Heysch, J., Ladoux, B., and Dufour, S. (2012). E-cadherin-dependent stimulation of traction force at focal adhesions via the Src and PI3K signaling pathways. Biophys. J. *103*, 175–184. https://doi.org/10.1016/j.bpj.2012.06.009.

60. Mertz, A.F., Che, Y., Banerjee, S., Goldstein, J.M., Rosowski, K.A., Revilla, S.F., Niessen, C.M., Marchetti, M.C., Dufresne, E.R., and Horsley, V. (2013). Cadherin-based intercellular adhesions organize epithelial cell-matrix traction forces. Proc. Natl. Acad. Sci. USA *110*, 842–847. https://doi.org/10.1073/pnas.1217279110.

61. Le Borgne-Rochet, M., Angevin, L., Bazellières, E., Ordas, L., Comunale, F., Denisov, E.V., Tashireva, L.A., Perelmuter, V.M., Bièche, I., Vacher, S., et al. (2019). P-cadherin-induced decorin secretion is required for collagen fiber alignment and directional collective cell migration. J. Cell Sci. *132*. https://doi.org/10.1242/jcs.233189.

62. Walko, G., Castañón, M.J., and Wiche, G. (2015). Molecular architecture and function of the hemidesmosome. Cell Tissue Res. *360*, 529–544. https://doi.org/10.1007/s00441-015-2216-6.

63. Sanghvi-Shah, R., and Weber, G.F. (2017). Intermediate filaments at the junction of mechanotransduction, migration, and development. Front. Cell Dev. Biol. *5*, 81. https://doi.org/10.3389/fcell.2017.00081.

64. Wang, W., Zuidema, A., Te Molder, L., Nahidiazar, L., Hoekman, L., Schmidt, T., Coppola, S., and Sonnenberg, A. (2020). Hemidesmosomes modulate force generation via focal adhesions. J. Cell Biol. *219*, e201904137. https://doi.org/10.1083/jcb.201904137.

65. Bonakdar, N., Schilling, A., Spörrer, M., Lennert, P., Mainka, A., Winter, L., Walko, G., Wiche, G., Fabry, B., and Goldmann, W.H. (2015). Determining the mechanical properties of plectin in mouse myoblasts and keratinocytes. Exp. Cell Res. *331*, 331–337. https://doi.org/10.1016/j.yexcr.2014.10.001.

66. Na, S., Chowdhury, F., Tay, B., Ouyang, M., Gregor, M., Wang, Y., Wiche, G., and Wang, N. (2009). Plectin contributes to mechanical properties of living cells. Am. J. Physiol. Cell Physiol. *296*, C868–C877. https://doi.org/10.1152/ajpcell.00604.2008.

67. Aman, A., and Piotrowski, T. (2008). Wnt/beta-catenin and Fgf signaling control collective cell migration by restricting chemokine receptor expression. Dev. Cell *15*, 749–761. https://doi.org/10.1016/j.devcel.2008.10.002.

68. Ferrer-Vaquer, A., Piliszek, A., Tian, G., Aho, R.J., Dufort, D., and Hadjantonakis, A.K. (2010). A sensitive and bright single-cell resolution live imaging reporter of Wnt/ß-catenin signaling in the mouse. BMC Dev. Biol. *10*, 121. https://doi.org/10.1186/1471-213X-10-121.

69. Vaezi, A., Bauer, C., Vasioukhin, V., and Fuchs, E. (2002). Actin cable dynamics and Rho/Rock orchestrate a polarized cytoskeletal architecture in the early steps of assembling a stratified epithelium. Dev. Cell *3*, 367–381.

70. Swat, M.H., Thomas, G.L., Belmonte, J.M., Shirinifard, A., Hmeljak, D., and Glazier, J.A. (2012). Multi-scale modeling of tissues using CompuCell3D. Methods Cell Biol. *110*, 325–366. https://doi.org/10.1016/B978-0-12-388403-9.00013-8.

71. Costa, A., Kieffer, Y., Scholer-Dahirel, A., Pelon, F., Bourachot, B., Cardon, M., Sirven, P., Magagna, I., Fuhrmann, L., Bernard, C., et al. (2018). Fibroblast heterogeneity and immunosuppressive environment in human breast cancer. Cancer Cell *33*, 463–479.e10. https://doi.org/10.1016/j.ccell.2018.01.011.

72. Wagner, J., Rapsomaniki, M.A., Chevrier, S., Anzeneder, T., Langwieder, C., Dykgers, A., Rees, M., Ramaswamy, A., Muenst, S., Soysal, S.D., et al. (2019). A single-cell atlas of the tumor and immune ecosystem of human breast cancer. Cell *177*, 1330–1345.e18. https://doi.org/10.1016/j.cell.2019.03.005.

STAR★METHODS

KEY RESOURCES TABLE

REAGENT or RESOURCE	SOURCE	IDENTIFIER
Antibodies		
P-cadherin	Invitrogen	Cat# MA1-2003; RRID: AB_2077774
P-cadherin	Thermofisher	Cat# 132000z
Collagen 17 (COL17)	Invitrogen	Cat# PA5-1033778
Keratin 14 (K14)	Biolegend	Cat# 905301; RRID: AB_2565048
Laminin-α3	Dr. Takako Sasaki	1110
Laminin-γ2 (Alexafluor 647)	Millipore Sigma	Cat# MAB19562- AF647
0FFD-actin	Sigma-Aldrich	Cat#A1978
Anti-rabbit IgG, HRP-linked antibody	Cell Signaling Technology	Cat# 7074S
Anti-mouse IgG, HRP-linked antibody	Cell Signaling Technology	Cat# 7076S
Alexa Fluor 488 goat anti-rabbit IgG (H+L)	Invitrogen	Cat# A11008
Alexa Fluor 594 goat anti-rabbit IgG (H+L)	Invitrogen	Cat# A11012
Alexa Fluor 594 goat anti-rat IgG (H+L)	Invitrogen	Cat# A-11007
DAPI (4',6-Diamidino-2-2Phenylindole, Dihydrochloride)	Thermofisher	Cat#: D1306
β-Catenin	Santa Cruz	Cat# sc-7963; RRID: AB_626807
Phospho-FAK.Y397	Cell Signaling	Cat# 8556; RRID: AB_10891442
FAK	Cell Signaling	Cat# 3285; RRID: AB_2269034
Phospho-Src.Y416	Cell Signaling	Cat# 6943; RRID: AB_10013641
Src	R&D System	Cat# AF3389; RRID: AB_2196155
TCF4	Millipore	Cat# CS204338
Mouse IgG	Millipore	Cat# 12-371B; RRID: AB_2617156
Goat anti-rabbit Fab fragment	Jackson ImmunoResearch	Cat# 111-007-003; RRID: AB_2337925
Rabbit anti-rat antibody	Vector Al	Cat# 4001
3-amino-9-ethylcarbaole (AEC)	Abcam	Cat$ Ab64252
ITG 0FFD1	BD Pharmingen	Cat# 553715
Fxycle Violet	Thermofisher	Cat# F10347
Cdh3-PE	R&D systems	Cat# FAB761P; RRID: AB_2291533
PDGFRb-PE-Cy7	Thermofisher	Cat# 25140282
Thy-1.1-PE-Cy7	Thermofisher	Cat# 25090082
Bacterial and virus strains		
pGFP-C-shLenti-Cdh3 (human)	Origene	Cat# TL314033
pRFP-C-shLenti-Cdh3 (mouse)	Origene	Cat# TL500332
pGFP-C-shLenti-scramble (human)	Origene	Cat# TR30021
pRFP-C-shLenti-scramble (mouse)	Origene	Cat# TR30032
pLKO.1-puro-laminin⍺3 (mouse)	Sigma Aldrich	Cat# XM_140451
pLKO.1-puro-scramble (mouse)	Sigma Aldrich	Cat# SHC016
pGFP-C-shLenti-scramble (mouse)	Origene	Cat# TR30021
pGFP-C-shLenti-laminin⍺3 (human)	Origene	Cat# TL311804
Biological samples		
Human tissue microarray	Washington University in St Louis	N/A
Chemicals, peptides, and recombinant proteins		
DMEM high glucose	Gibco	Cat# 11995073
DMEM/F12	Gibco	Cat# 11330057
FBS	Corning	Cat# MT35011CV

(*Continued on next page*)

Continued

REAGENT or RESOURCE	SOURCE	IDENTIFIER
Penicillin Streptomycin	Gemini	Cat #400-109
Trypsin/EDTA	Gibco	Cat # 25300054
Trypsin	Gibco	Cat# 27250-018
Collagenase A	Sigma	Cat# C5138
Rat tail Collagen 1	Corning	Cat# CB354249
Matrigel	Corning	Cat# CB40230C
Laminin-332	Biolumina	Cat# LN332-0502
DPBS	Gibco	Cat# 14190250
Gentamicin	Gibco	Cat# 15710064
Bovine Insulin	Gemini Bioproducts	Cat# 700-112P
DNAse	Sigma	Cat# D4263
Polybrene	Sigma	Cat# 107689
Bovine Serum Albumin	Sigma	Cat# A7906
4'6-Diaminidin-2-phenylindol (DAPI)	Sigma	Cat # D9542
Paraformaldehyde (PFA)	Fisher Scientific	Cat # 50-980-487
Tween 20	Sigma	Cat # P9416
FGF	Sigma	Cat# F0291
SDF1	Sigma	Cat# SRP3276
Insulin, transferrin, sodium selenite (ITS)	Gibco	Cat # 41400-045
Formalin	VWR	Cat # 16004-128
Vectashield	Vector Laboratories	Cat # H-1200-10
SYBR Green PCR Master Mix	Applied Biosystems	Cat # 4367659
Bradford Reagent	Biorad	Cat # 5000205
SuperSignal West Pico Plus Chemiluminescent Substrates	ThermoFisher	Cat# 34580
SuperSignal West Femto Chemiluminescent Substrates	ThermoFisher	Cat # 34095
Trizma base	Sigma	Cat# T6066
Glycine	Fisher Scientific	Cat# BP3811
EDTA	Fisher Scientific	Cat# BP120500
Tris-HCl	Quality Biological	Cat# 351-006-131
NaCl	Sigma	Cat # 746398
SDS	Sigma	Cat # L3771
NaHCO3	Sigma	Cat # S5761
Proteinase K	Sigma	Cat # P6556
Hematoxylin	DAKO	Cat # S3301
Critical commercial assays		
RNeasy Plus mini kit	Qiagen	Cat# 74134
NE-PER Nuclear and Cytoplasmic Extraction Reagens	ThermoFisher	Cat# 78833
Chromatin Immunoprecipitation Assay	Millipore	Cat # 17-295
HEMA3 staining kit	Fisher	Cat # 22-122911
Deposited data		
Single cell RNA sequencing	NCBI	Ascension numbers: GSE171203
Mathematical Modeling Code	GitHub	https://doi.org/10.5281/zenodo.7349226
Experimental models: Cell lines		
Human BT549	ATCC	Cat# HTB-122

(*Continued on next page*)

Continued

REAGENT or RESOURCE	SOURCE	IDENTIFIER
Mouse 4T1	ATCC	Cat# CRL-2539
Experimental models: Organisms/strains		
Mouse: MMTV-PyMT (FVB/n)	Jackson laboratory	RRID: IMSR_JAX:001800
Mouse: K14-GFP; MMTV-PyMT (FVB)	Vaezi et al.[69]	NA
Mouse: Balb/cJ	Jackson laboratory	RRID: IMSR JAX:000651
Mouse: PDX donor	Jax laboratories	JAX: 000080739
Mouse: immunodeficient gamma (NSG)	Jax laboratories	JAX: 005557
PCR Oligonucleotides		
Laminin α3 mouse Forward: 5' -ACACCTG GGACGTGGATTG- 3'	This paper	N/A
Laminin α3 mouse Reverse: 5' -CTTGCAGG GTGAATGCTTCAT- 3'	This paper	N/A
Laminin π3 mouse Forward: 5' -GGCTGC CTCGAAATTACAACA- 3'	This paper	N/A
Laminin π3 mouse Reverse: 5' -ACCCT CCATGTCTTGCCAAAG- 3'	This paper	N/A
Laminin ψ2 mouse Forward: 5' -CAGACAC GGGAGATTGCTACT- 3'	This paper	N/A
Laminin ψ2 mouse Reverse: 5' -CCACGT TCCCCAAAGGGAT- 3'	This paper	N/A
Cadherin-3 mouse Forward: 5' -CTGGAG CCGAGCCAAGTTC- 3'	This paper	N/A
Cadherin-3 mouse Reverse: 5' -GGAGTG CATCGCATCCTTCC- 3'	This paper	N/A
π-actin mouse Forward: 5' -GGCTGT ATTCCCCTCCATCG- 3'	This paper	N/A
π-actin mouse Reverse: 5' -CCAGTT GGTAACAATGCCATGT- 3'	This paper	N/A
Laminin α3 human Forward: 5' - CACC GGGATATTTCGGGAATC - 3'	This paper	N/A
Laminin α3 human Reverse: 5' - AGCT GTCGCAATCATCACATT - 3'	This paper	N/A
Laminin π3 human Forward: 5' - GCAG CCTCACAACTACTACAG- 3'	This paper	N/A
Laminin π3 human Reverse: 5' - CCAG GTCTTACCGAAGTCTGA- 3'	This paper	N/A
Laminin ψ2 human Forward: 5' - CAAAG GTTCTCTTAGTGCTCGAT - 3'	This paper	N/A
Laminin ψ2 human Reverse: 5' - CACTTG GAGTCTAGCAGTCTCT - 3'	This paper	N/A
Cadherin-3 human Forward: 5' -ATCATC GTGACCGACCAGAAT- 3'	This paper	N/A
Cadherin-3 human Reverse: 5' -GACTC CCTCTAAGACACTCCC- 3'	This paper	N/A
π-actin human Forward: 5' - CATGTAC GTTGCTATCCAGGC - 3'	This paper	N/A
π-actin human Reverse: 5' - CTCCTTA ATGTCACGCACGAT - 3'	This paper	N/A
Recombinant DNA		
Mouse Laminin α3 shRNA 5' – ATCCAGTGGCTGGCAATATAA – 3'	This paper	N/A
Human Laminin a3 shRNA 5' – ACGGCCTACGAGAACATCCTCAATGCCAT – 3'	This paper	N/A

(*Continued on next page*)

Continued

REAGENT or RESOURCE	SOURCE	IDENTIFIER
Mouse Cadherin-3 shRNA 5' – TGAGGACGATGCTGTCAACACTTACAATG – 3'	This paper	N/A
Human Cadherin-3 #1 5' – ATGACTTCACTGTGCGGAATGGCGAGACA – 3'	This paper	N/A
Human Cadherin-3 #2 5' – GCAGTAGTGGAGAT CCTTGATGCCAATGA – 3'	This paper	N/A
pCMV-VSV-G	Addgene	Cat# 8454
pCMV deltaR8.2	Addgene	Cat# 79047
Software and algorithms		
FIJI	Distribution of ImageJ	https://imagej.net/software/fiji/downloads
Zen Software	Zeiss	https://www.zeiss.ch/mikroskopie/produkte/mikroskopsoftware/zen.html
NIS-Elements Imaging	Nikon	https://www.microscope.healthcare.nikon.com/products/software/nis-elements
GraphPad Prism	GraphPad Software Inc	https://www.graphpad.com/scientific-software/prism/
Matlab	Mathworks	https://www.mathworks.com/products/matlab.html
Partek flow	Partek	https://www.partek.com/

RESOURCE AVAILABILITY

Lead contact

Further data and information about resources and reagents are available from the corresponding author, Gregory Longmore (glongmore@wustl.edu), upon reasonable request.

Materials availability

This study did not generate new unique reagents.

Data and code availability

- All data to support the findings of this study are included in the paper and the supplemental information. The scRNAseq raw-data is available at NCBI's Gene Expression Omnibus database. Accession numbers are listed in the key resources table.
- Mathematical modeling code has been deposited at github (see key resources table) and are publicly available as of the date of publication. DOI is listed in the key resources table.
- Any additional information required to reanalyze the data reported in this paper is available from the lead contact upon reasonable request.

EXPERIMENTAL MODEL AND SUBJECT DETAILS

Mouse Breast Tumor Models

All mice were used in compliance with the Washington University's Institutional Animal Care and Use Committee and approved under protocol #20150145. Mice colonies were maintained in individually ventilated cage (IVC) systems under specific pathogen-free conditions and received food and water ad libitum.

Mouse MMTV-PyMT mice were obtained from The Jackson Laboratory. They develop multifocal primary breast tumors that are highly invasive and exhibit high (>90%) metastatic propensity. Genetically they resemble human luminal B breast tumors. MMTV-PyMT mice (FVB/n) were crossed to K14-Actin.GFP mice (FVB/n), which is a transgenic mouse expressing an Actin.GFP fusion protein under the control of the keratin-14 promoter, to generate K14-GFP tagged MMTV-PyMT mice. The transgene is functional in mitotically active epidermal cells[69] and the endogenous K14 gene is not altered in these mice. We refer to all K14-positive cells obtained from this mouse as "K14-GFP." Tumor-bearing mice were monitored weekly and euthanized at 12 weeks. PyMT alleles were detected by PCR using primers 5'- GGA AGC AAG TAC TTC ACA AGG G -3' (forward) and 5'- GGA AAG TCA CTA GGA GCA

GGG -3' (reverse). GFP expression was detected using fluorescence microscopy using Nikon upright fluorescent microscope. K14-Actin.GFP; MMTV-PyMT females developed mammary tumors and were subsequently used for experiments in this study.

Human patient derived triple negative (TNBC – ER negative, PR negative, HER2 negative) metastatic xenograft (PDX) donor mice were obtained from JAX laboratories (JAX J000080739; JAX laboratories have informed consent for taking patient tissues for the human cells used in the commercially available PDX donor mice purchased. These were serially passaged via breast implantation into the fourth mammary fat pads of immunodeficient gamma (NSG) mice.

4T1 syngeneic orthotopic breast transplant model: Eight-week old female BALB/cJ mice (Jackson Labs) were anaesthetized with a ketamine/xylazine cocktail (90 mg/kg, 1 ketamine and 13 mg/kg, xylazine, intraperitoneal injection) and the abdomen was sterilized using povidone iodine (Betadine) solution and ethanol. A small Y-shaped incision was made in the lower abdominal skin to expose the fourth mammary gland using surgical scissors and bleeding vessels were cauterized. 4T1 cells (1×10^6) in 50 μl DMEM were injected into the fourth mammary gland using a 29-gauge needle. The skin flaps were replaced and closed using 9mm wound clips, and the surgical site was swabbed with triple-antibiotic cream. Primary tumors and lungs were collected at end stage (primary tumor @ 2cm) and processed for immunohistochemistry and mRNA preparation. To do so, lungs and primary tumors were then fixed in 10% formalin for 24 h, cryopreserved in 30% sucrose overnight, and finally embedded in OCT and frozen in a dry ice/ethanol bath. Lungs were processed in three step-sections of 50 um with two serial sections of each step. Metastatic tumor nodules were counted and averaged per lobe of lung (5 lobes) per mouse. Primary breast tumors were also stained for laminin 332, and gene expression for Cdh3 and Lamα3, Lamβ3, and Lamγ2 determined via Q-PCR.

Breast tumor cell lines

Human invasive and metastatic breast cancer BT549 and mouse invasive and metastatic breast cancer 4T1 cells were purchased from the American Type Culture Collection (ATCC; Masassas VA) and cultured in Dulbecco's modified Eagle's medium (DMEM) with 10% serum and penicillin-streptomycin. Both cell lines express K14, Cdh3, and make Laminin. Cells were routinely checked for the presence of mycoplasma by polymerase chain reaction (PCR) amplification using primers Myco + (5′-GGG AGC AAA CAG GAT TAG ATA CCC T-3′) and Myco− (5′-TGC ACC ATC TGT CAC TCT GTT AAC CTC-3′) every 6 months. Only mycoplasma-negative cells were used in these studies. 4T1 cells were cultured either diffusely – non-contacted (30% plate coverage) or confluent – cell-cell contacted. To make cell spheroids (aggregates) for 3D culture, cells were cultured on low adhesion plates (Corning) to naturally form spheroids, single cells were filtered out, and then spheroids loaded into the microfluidic devices as with MMTV-PyMT breast tumor organoids.

METHOD DETAILS

Computational model

We used a Cellular Potts approach to model heterogeneous tumor organoid migration in 3D because it is efficient in defining deformable 3D cell bodies. We model a collection of biological cells by attaching to each lattice point (pixel) $(i;\ j)$ of a square lattice a label σ_{ij}, which identifies the corresponding cell, and a label $\tau(\sigma_{ij})$, which identifies cell type. Adjacent lattice sites are defined to lie within the same cell if they have the same value of σ_{ij}. The system evolves by the random movement of individual pixels subject to transition probabilities based on the Monte Carlo method.[70] At each Monte Carlo Step, two neighboring pixels are chosen randomly, with one as source pixel and the other as target pixel. If both pixels belong to the same cell $(i.e.,\sigma(source) = \sigma(target))$, then no changes are made to the lattice. Otherwise, the source pixel attempts to occupy the target pixel based on Monte Carlo acceptance probability, which is calculated from the difference in total system energy. We evaluate the total system energy associated with the configuration before the move and after the move as per the following equation:

$$E = \sum_{\forall i,j;\ \sigma_i \neq \sigma_j} J_{\tau(\sigma(i)),\tau(\sigma(j))} + \sum_{\forall cells} K_a(V_0 - V)^2 + \sum_{\forall cells} K_p(A_0 - A)^2 + \sum_{\forall cells} P_{cell} \qquad \text{(Equation 1)}$$

Here, $J_{\tau(\sigma(i)),\tau(\sigma(j))}$ represents contact energy for the two cell types in contact $(\tau(\sigma(i)),\tau(\sigma(j)))$.

The first term represents contribution from the total energy due to cell-cell adhesions. Second and third terms represent contributions from bulk elasticity of the cell and cell-surface contractility, respectively. $K_a$and K_p are constants for bulk elasticity and contractility, respectively. V_0 and A_0 are target volume and surface area that the cell has in isolation. P_{cell} represents effective protrusive energy of a cell (discussed ahead). After calculating energy of system before (E_i) and after (E_f) the copy attempt will always be successful if $E_f < E_i$, *i.e.* $\Delta E < 0$. If $\Delta E \geq 0$, the copy attempt is accepted with a probability of $e^{-\left(\frac{\Delta E}{T}\right)}$. Higher values of T would tend to accept more unfavorable copy attempt. Here, we extend the Potts framework to model cellular invasion. We assign an effective protrusive energy to each cell, dependent on its cell type and interaction with its neighboring cells and ECM (spaces not occupied by the cell are assumed to belong to ECM).

Organoids were modeled as a spherical collection of cells with 10% leader cells (green) mixed randomly with non-leader "follower" cells (blue) (Figures 1A and 1B). Adhesions are annotated as dotted lines, where J_{FF} represents follower-follower adhesion energy (cyan) and J_{LF} represents leader-follower adhesion energy (red). Based on our experiments done on primary organoids in a uniform chemokine gradient, we assume that leader cells sense the defined chemokine gradient and extend protrusions in that direction. We define leader cell protrusive force P_L (a dimensionless quantity) as following:

$$P_L = \begin{cases} P_{L,0}, \textit{No ECM contact} \\ P_{L,0}\left(1 - e^{-\frac{F_{act}}{F_{res}}}\right), \textit{In contact with ECM} \end{cases} \quad \text{(Equation 2)}$$

Here, $P_{L,0}$ is the inherent protrusive force of leader cells without any feedback from the ECM. When leader cells encounter the ECM, such as an organoid invading into collagen, there are two counteracting mechanisms that alter this effective protrusive force produced by leader cells. First, the ECM serves as a steric barrier causing a resistance force F_{res}, which lowers effective leader cell protrusive force due to ECM density and crosslinking. Second, cell-ECM adhesions are expected to activate mechanotransductive signaling and remodel the collagen matrix via degradation or fiber alignment. These leader cell-ECM interactions are assumed to produce an active force F_{act} that works against the ECM resistance force. Without this active force, ECM resistance would simply stop any invasion due to passive ECM resistance. We write this active force as:

$$F_{act} = \beta f n \quad \text{(Equation 3)}$$

Here, n is the fraction of leader cells engaged with the ECM ($\beta \sim 1$)and f is force per leader cell. $\frac{f}{F_{res}} = 5$. The degree of ECM feedback β is defined as a sigmoidal Hill function in term of the area of the leader cell in contact with the ECM as following:

$$\beta = \frac{(A)^4}{(A)^4 + A^{*4}} \quad \text{(Equation 4)}$$

Here, A is the area of the leader cell in contact with the ECM relative to the total cell area and $A^* = 0.05$ is a calibration constant. Based on this function, $\beta = 0$ when leader cells are within the organoids and β quickly rises to 1 as it interacts with the ECM, thus causing the active ECM feedback defined in Equation 3.

In our model, follower cells are assumed not to follow the chemokine gradient, i.e., they are permitted to randomly polarize in any direction. We also assume an overall mechanical and chemical communication between follower and leader cells. Thus, follower cell protrusive force depends on average leader cell force, defined as:

$$P_F = \sum_{\forall Leaders} \beta \cdot P_L \Big/ \sum_{\forall Leaders} \beta \quad \text{(Equation 5)}$$

This average P_F is assigned to all follower cells.

Calibrating cell-cell adhesions in Potts modeling

Since our model can independently define leader and follower cell adhesions, there are many possible combinations of leader-leader, leader-follower, and follower-follower adhesions. To understand their relative contributions in a systematic manner, we fixed leader-leader adhesion strength as moderate, $J_{LL} = 5$, and analyzed organoid configuration after 4 hours for four adhesion cases (Figures 1D and 1E; Videos S1B, S2A, S2B, and S3A). Case (*i*): strong leader-follower ($J_{LF} = 1$) and weak follower-follower ($J_{FF} = 10$) adhesions made it more energetically favorable to maintain leaders with followers while followers scatter, which reduced leader cell polarization and broke up the organoid (Figures 1C and 1Di; Video S1B). Case (*ii*): weak leader-follower ($J_{LF} = 10$) and strong follower-follower ($J_{FF} = 1$) adhesions reduced organoid scattering, but leader cells exited the organoid after frontward polarization (Figures 1C and 1Dii; Video S2A). Case *(iii)*: both leader-follower and follower-follower weak adhesions ($J_{FF} = J_{LF} = 10$) allowed for leader cell polarization but the organoid dissociated and leader cells exited the organoid (Figures 1C and 1Diii; Video S2B). Thus, if either leader-follower or follower-follower adhesions (J_{LF}, J_{FF})were weak, the organoid integrity was compromised. In Case (*iv*), upon setting strong leader-follower and follower-follower adhesions ($J_{LF} = J_{FF} = 1$), the organoid remained intact, leader cells polarized to the front, and they did not exit the organoid (Figures 1C and 1Div; Video S3A), which captured organoid morphology, yet organoid displacement remained low. Based on these parametric scans, we set moderate leader-leader adhesions ($J_{LL} = 5$) and strong follower-follower and leader-follower adhesions ($J_{LF} = J_{FF} = 1$). To analyze the effect of leader protrusive forces, we varied P_L from 1 to 20 and observed organoid configuration after 16 hours (Figure 1F). With increasing leader protrusions, we predict increasing leader cell polarization, decreasing organoid circularity, and increasing organoid displacement (Figures 1F and 1H). However, even for the highest value of $P_L = 20$, the organoid became highly elongated and predicted organoid movement was minimal relative to its size (Figures 1F and 1H; Video S3B).

Primary breast tumor organoid isolation and culture

Mouse PyMT primary mammary tumor organoids were isolated from @12 week old tumor bearing mice[18] and were immediately mixed with collagen I (2 mg/ml, Corning) and loaded into the middle chamber of the microfluidic device.[28] Organoids are roughly 200-500 cells each. Collagen was allowed to polymerize (37°C, 1h, 20% O_2), and media (DMEM, 10% FBS, P/S) delivered to the top and bottom fluidic lines and cultured in 2% O_2 for 48 hours. At no time were the isolated tumor organoids exposed to plastic tissue culture dishes.

In other experiments we used "standard breast tumor organoid cultures[18]". Briefly, tumor organoids were embedded in 2 mg/ml collagen 1 solution (2-3 organoids/μl), and 100 μl suspension was plated in 4-well coverslip-bottomed chambers. Samples were placed on a 37^{0}C heat block (30 min), followed by incubation at 37^{0}C (30 min) to allow polymerization, and cultured in 1 ml of 2.5nM FGF2/EGF or SDF1 in organoid media under normoxia.[25]

For human-in-mouse PDX derived TNBC metastatic xenograft (PDX) donor mouse model, tumor growth was monitored weekly and visible after eight weeks. When tumors reached @ 1 cm, mice were euthanized, and organoids obtained. These organoids were then handled and treated in the same manner as the mice mammary tumor organoids, described above.

For studies using Laminin 332, we encapsulated PyMT breast tumor organoids or 4T1 spheroids in a 1:1 ratio of collagen I (2mg/ml) to Laminin 332 (0.1 mg/ml, Biolumina). To promote directed collective migration, we generated a chemokine chemical gradient of SDF1 (0.05 ug/ml, Sigma-Aldrich) or interstitial fluid flow gradient (12 μm/s) via the top fluidic line.[28]

Representative videos of the computational simulations can be found in the following supplemental movies: Videos S1A and S1B - Differential leader and follower cell adhesions (corresponds to Figure 1), Videos S2A and S2B - Parametric scans for various combinations of differential leader and follower cell adhesions (corresponds to Figure 1), Videos S3A and S3B – Parametric scans for various combinations of differential leader and follower cell adhesions plus progressively higher leader cell protrusions (corresponds to Figure 1), and Video S4 – Added ECM adhesion feedback with varying leader protrusive forces (corresponds to Figure 1).

Primary breast organoid reconstitution assay

K14-Actin.GFP; MMTV-PyMT mouse breast tumors were isolated down to the single cell level using sequential collagenase followed by trypsin digestion. Single cells were strained (70 μm) to remove any debris or remaining cell clusters and stained for live/dead (FxCycle Violet). Cdh3-PE (R&D systems), PDGFRβ-PE-Cy7 (ThermoFisher), and Thy-1.1-PE-Cy7 (ThermoFisher) antibodies were used for sorting. FACS sorting (BD Aria II) was performed in a sequential order: first, cells were gated for live cells, second, cells were gated to remove CAFs (PDGFRβ and Thy-1.1) and CD45+ immune cells, and finally cells were gated to sort for K14+/Cdh3+ cells. K14+/Cdh3+ cells were mixed with normal mammary gland (MG) organoids and cultured in low-adhesion well plates (Corning) overnight (37°C, 20% O_2) to form "MG+K14$^+$/Cdh3$^+$" organoids. Normal mammary gland organoids were isolated from syngeneic female wild-type FVB/n age-matched mice and digested to the organoid level using collagenase 1 solution.[25,28]

Single cell RNA sequencing (scRNAseq) and analysis

Primary breast tumor organoids were isolated from the microfluidic devices after 48 h or hypoxia (no signal) or after promoting collective migration within microfluidic devices in response to a SDF1 chemokine chemical gradient or interstitial (IF) flow gradient; 18 hours; average 150 μm length of directional migration[28]). Organoids were extracted from the device and isolated down to the single cell level by delivering a low concentration collagenase/trypsin digestion. After successful extraction, cells were stained for live/dead (FxCycle Violet; ThermoFisher), and live cells sorted via FACs (BD FACSAria II). After sorting, cells were centrifuged and resuspended in scRNA sequencing buffer and final concentration was adjusted to 1000 cells/ul and sent for scRNA processing (10X Genomics). Samples were processed with each library sequenced on 0.125 NovaSeq S4 flow cell (300 cycles; 1.000 flow cell total). Read alignment, gene expression estimation, normalization and quality control were performed using the Cell Ranger Single-Cell Software Suite (10x Genomics). Cell Ranger count was used to align samples to the reference genome (mm10), quantify reads and filter reads with a quality score below 30.

scRNAseq analysis yielded data from 1500-2000 cells with a coverage of ~125,000 read pairs per cell. All single cell RNA-sequencing (scRNAseq) data were analyzed using Partek Flow software. For quality control, nuclei with mitochondrial content >5% were removed. Nuclei that are doublets or multiplets were filtered out by two steps. First, nuclei with more than one marker gene expressed were removed. Then cells with high UMI and gene number per cell were filtered out. UMI counts were normalized following Partek Flow recommendations: for each UMI in each sample the number of raw reads was divided by the number of total mapped reads in that sample and multiplied by 1,000,000, obtaining a count per million value (CPM), the normalized expression value was log-transformed (pseudocount = 1). Starting from the normalized data node, we performed clustering analysis for each sample separately by means of graph-based clustering which employs the Louvain algorithm. Clustering analysis was done based on the first 100 principal components. To visualize single cells in a two-dimensional space, we performed a uniform manifold approximation and projection (UMAP) dimensional reduction using the first 20 principal components for each sample separately and for the entire data set.

To identify various cell types present we utilized graph-based clustering of transcripts, the ImmGen database, and published gene markers. We identified marker genes for each identified cell group by computing ANOVA comparing each cluster to all the other cells in the data set to obtain a list of genes with fold change (FC) >2 ranked according to ascending p-value. Using the list of genes generated for each cluster, we compared with known gene markers for various cell sub-types based on recently published data sets.[24,33,71,72] We also performed differential expression of genes between cell clusters within a sample using ANOVA analysis and considered genes with FC>2 or FC<-2 and p-value <0.05 as differentially expressed.

Differentially expressed genes between the different groups (no migration, SDF1 gradient, and interstitial fluid flow) are listed in Table S1 - Differentially expressed genes from single cell sequencing analysis from no migration, SDF1 chemokine gradient, and interstitial fluid flow groups.

shRNA lentiviral depletion of gene expression

For each gene targeted (mouse and human), we synthesized 5 different shRNA lentivirus particles – both human and mouse specific Cdh3 (Origene, TR30023 (human), TL500332 (mouse)) and Laminin α3 (Sigma-Aldrich), as well as corresponding scramble (shSCR) controls. shRNA sequences used are listed in key resources table and Table S2. Each lentivirus also expressed either GFP or RFP that allowed for identification and quantification of transduced cells. Human BT549 breast tumor cells and mouse 4T1 breast tumor cells were used to screen the various lentiviruses for efficient protein depletion (>80%). Successful transduction was also confirmed by visualized GFP/RFP expression. For each gene 2 distinct shRNAs were used for subsequent functional studies: one targeting the mouse gene and one targeting the human gene.

Mouse MMTV-PyMT primary breast tumor organoids and human-in mouse PDX primary breast tumor organoids embedded in 3D collagen I within the microfluidic devices were transduced with shRNA expressing lentiviruses directly via fluidic lines. Organoids were exposed to transduction media for 16 hours, and successful transduction confirmed by visualizing fluorescence marker expression. Organoids began to express GFP/RFP after 18 hours. Organoids were immunostained, in the microfluidic device, for Cdh3 and Laminin 332 (mouse) or Laminin 5γ2 (human) expression to confirm successful knockdown.

Transwell Invasion Assay

Transwell invasion assays were performed using a 24-well polycarbonate membrane (Corning) with 8.0 μm pore size. The upper chambers were precoated with 1 mg/ml Matrigel and incubated at 37 °C for 2 h. The cells (5×10^4/well) in DMEM containing 1% FBS were seeded into the upper chambers, and 600 μl of DMEM with 10% FBS was added to the lower chambers. After incubation for 24 h at 37 °C, polycarbonate membranes were stained with HEMA3 staining kit (Fisher). BT549 or 4T1 cells on the upper surface were removed with cotton-tipped swabs. The number of invasive cells were counted from six randomly selected visual fields using compound light microscopy (200x magnification).

3D Cell Invasion Assay

For 3D cell invasion assays, 10^5 cells (BT549 or 4T1) were embedded in 20 μl of type I collagen gel (2.2 mg/ml, Corning). After gelling, the plug was embedded in a cell-free collagen gel (2.2 mg/ml) within a 24-well plate. After allowing the surrounding collagen matrix to gel (1 h at 37°C), 0.5 ml of culture medium was added to the top of the gel and cultured for another two days. Invasion distance from the inner collagen plug into the outer collagen gel was quantified.

Live-cell imaging and analysis

After culturing organoids for 48 hours in 2% O_2, we induced collective migration and performed live-cell imaging (Nikon Ti-E, 10x, 40x, 60x; controlled temperature, humidity, and oxygen (2% O2)). Each organoid within the device was marked using Nikon Imaging software, and pictures were taken every 20 minutes for a maximum of 18 hours. After imaging, devices were used for immunofluorescence labeling and imaging, or organoids were extracted from the device for single cell sequencing analysis.

Image analysis was performed using Metamorph, Matlab, and FIJI to quantify organoid migration efficiency (%) in the direction of the gradient,[28] average velocity (μm/min), and direction of travel (migration maps). We also tracked and quantified K14-GFP localization over time. At various time points, images of organoids were divided into top (front; direction of migration) and bottom (back) halves, and total K14-GFP fluorescence of each half was calculated using FIJI and the following formula: cell fluorescence = integrated density – (area of half x mean fluorescence of background).

Immunofluorescence of breast tumor organoids

All immunostaining was performed after imaging studies with organoids maintained within the devices, and all reagents were delivered via microfluidic lines. After fixing and blocking, organoids were stained for Cadherin-3 (ThermoFisher), Collagen 17 (ThermoFisher), activated Integrin β1 (9EG7; BD Biosciences), mouse Laminin 332 (gift from Dr. Takako Sasaki, OITA University), or human Laminin5 γ2 (EMD Millipore); all primary antibody staining was incubated overnight at 4°C. Species-specific secondary antibodies (488, 555, or 633 wavelength) and nuclei staining (DAPI) were also used. Imaging was performed via confocal microscopy (Zeiss, 63X).

Tumor tissues were fixed with 10% formalin for 24 h, embedded in paraffin and sectioned (5 μm). After dewaxing using a graded alcohol series and antigen retrieval, the tumor slides were treated with 3% hydrogen peroxide, and then blocked with 10% normal goat serum for 1 h. The slides were incubated with the primary antibodies against Laminin-α3 (1:500) at 4°C overnight. After three washes with PBS, the tissue sections were incubated with goat anti-rabbit AlexaFluor 594 antibody (Invitrogen) for 2h at 4°C. Slides were then mounted using VECTASHIELD (Vector Laboratories) with DAPI and coverslips applied.

Gene expression

Total RNA was extracted from cell lines or primary tumor tissues by RNeasy Plus Mini Kit (Qiagen). Subsequently, RNA was reverse transcribed into cDNA using the SuperScript First-Strand Synthesis System for RT-PCR (Invitrogen). cDNA was amplified using SYBR Green PCR Master Mix (Applied Biosystems) on QuantStudio 3 Real-Time PCR System (Applied Biosystems). The primers targeted Lamα3, Lamβ3, Lamγ2, Cdh3 and β-actin are listed in key resources table. The thermocycling conditions were as follows: initial denaturation at 95°C for 10 min, 40 cycles of 95°C for 15s, 60°C for 60s. β-actin was chosen as an endogenous control. The $2-\Delta\Delta CT$ method was used to calculate the relative mRNA levels.

Protein expression

Cells were lysed in RIPA buffer plus protease inhibitors (Sigma-Aldrich). Protein concentration was measured using Bradford Reagent (Biorad). Lysates were subjected to SDS-PAGE, transferred to PVDF membranes, blocked in 5% milk, incubated with primary antibody overnight, secondary antibody for 2 hours and visualized using SuperSignal WestPico and/or Super Signal West Femto Chemiluminescent Substrates (ThermoFisher Scientific). Exposures were acquired using a ChemiDoc Imager (BioRad).

Subcellular fractionation

Nucleus and cytoplasm fractionation was performed with NE-PER Nuclear and Cytoplasmic Extraction Reagents (ThermoFisher Scientific Cat #78833). Briefly, cells were washed with PBS, scraped, and pelleted by centrifugation. Then, the cell pellet was resuspended in cytoplasmic extraction buffer supplemented with protease inhibitor and incubated on ice for 10 min. The cytosolic fraction was obtained as supernatant of sequential centrifugation for 5 min at 15,000rpm. For the nuclear fraction, the pelleted nuclei were resuspended in a Nuclear Extraction buffer containing protease inhibitors for 40 min on ice and collected as the supernatant of final centrifugation for 10 min at 15,000rpm. Lamin a/c detection was used as a marker of the nucleus; GAPDH detection was used as a marker of cytoplasm. Protein level was determined for each extracted fraction. To quantify Western blot results, all samples were normalized to equal number of cells at start of process.

Chromatin immunoprecipitation (ChIP) Assay

The Chromatin immunoprecipitation Assay was performed with commercial reagents (Millipore, Cat #17-295). In brief, confluent (cell-cell contacted) WT 4T1 cells were fixed with 1% formaldehyde at 37 °C for 10 min. and stopped with 100 mM glycine for 5min. After washing with PBS, cells were collected and lysed in SDS lysis buffer (1% SDS, 10 mM EDTA, 50 mM Tris, pH 8.1, supplemented with protease inhibitor), then sonicated into 200 to 1,000 bp fragments. Sonicated chromatin was diluted 10-fold with ChIP dilution buffer (0.01% SDS, 1.1% Triton X100, 1.2 mM EDTA, 16.7 mM Tris-HCl, pH 8.1, 167 mM NaCl), then incubated overnight 4°C with the following antibodies: β-catenin (mouse monoclonal, Cat# 7963, Santa Cruz), TCF-4 (mouse monoclonal, Cat# CS204338, Millipore). The normal mouse IgG (Cat# 12-371B, Millipore) was used as a negative control. The next day, 60 μl protein A agarose/Salmon Sperm DNA was added to each sample and incubated at 4°C for 1h, followed by four washes with wash buffer. The protein-DNA complexes were eluted with freshly prepared elution buffer (1%SDS, 0.1M $NaHCO_3$) and crosslink reversed (5M NaCl, 65°C for 4h) with subsequent addition of proteinase K (45°C for 1h). The DNA fragments were purified by phenol/chloroform extraction, followed by ethanol precipitation. Quantitative analysis of the DNA fragments was performed by SYBR Green qPCR. The qPCR data were analyzed by the fold enrichment method using $2^{-\Delta\Delta Ct}$ formula. Primers used are provided in Table S2 - Putative promoters of mouse Laminin 332 genes. The SP5 promoter was used as a positive control for β-catenin and TCF4 ChIP (Figure S6E).

Multiplex immunohistochemistry

A tissue microarray (2 mm cores) was generated from the primary tumors of untreated patients at Washington University who presented with metastatic disease. Six TNBC samples with significant tumor-stromal boundaries and 6 TNBC without significant tumor-stromal boundaries were analyzed.

TMA samples were stained on Leica BOND Automated IHC/ISH Stainer using BOND Polymer Refine Detection System in combination with goat anti-rabbit Fab fragment (Jackson ImmunoResearch 111-007-003, 1:25), rabbit anti-rat antibody (Vector AI-4001, 1:500), 3-Amino-9-ethylcarbazole (AEC) chromogenic substrate (Abcam ab64252) and hematoxylin (DAKO S3301). The TMA samples were first stained with anti-active ITGβ1 antibody (BD Pharmingen 553715, 1:300). After the staining was finished, the slide was mounted with aqueous mounting media (Vector H-5501) and scanned using Zeiss Axio Scan.Z1 slide scanner. The slide was then submerged in TBS-T buffer at 4 Celsius overnight to remove the coverslip. After 3 washes in diH_2O, the slide was incubated in 50% ethanol for 5 minutes and then transferred to acidified (1% HCl) 70% ethanol and incubated for 10 minutes with agitation to remove AEC chromogen and hematoxylin. The slide was then incubated with 100% ethanol for 15 minutes with agitation and was rehydrated and stored in TBS-T at 4 Celsius until next staining cycle. Such staining-scanning-stripping cycle was repeated for each of the following markers in the listed order: Cadherin-3 (Cell Signaling Technology 14029, 1:200), Laminin 5 γ2 (Sigma MAB19562-AF647, 1:150), and Cytokeratin 14 (Abcam ab7800, 1:1000). Scanned bright field images were deconvoluted into pseudo-fluorescent images and merged using HALO computational pathology software. The resulted images were analyzed using Indica Lab's HighPlex FL module on HALO.

QUANTIFICATION AND STATISTICAL ANALYSIS

For all organoid experiments we analyzed a minimum of 12 organoids from at least 3 different mice in the microfluidic devices. Assuming a 50% change between experimental and control groups, a 0.05 significance level and 0.80 power we estimated that we need at least 10 organoids per genotype per experimental condition. Although most alleles we study are on a pure FVB/n background, not all are, therefore, the use of 3 or more different mice controlled for potential phenotype-strain variability. All data was analyzed by t-test and ANOVA with Tukey's Post-hoc analysis using GraphPad Prism 8. Statistical details of experiments and parameters can be found in the figure legends and results.